



## 저작자표시-비영리-변경금지 2.0 대한민국

이용자는 아래의 조건을 따르는 경우에 한하여 자유롭게

- 이 저작물을 복제, 배포, 전송, 전시, 공연 및 방송할 수 있습니다.

다음과 같은 조건을 따라야 합니다:



저작자표시. 귀하는 원저작자를 표시하여야 합니다.



비영리. 귀하는 이 저작물을 영리 목적으로 이용할 수 없습니다.



변경금지. 귀하는 이 저작물을 개작, 변형 또는 가공할 수 없습니다.

- 귀하는, 이 저작물의 재이용이나 배포의 경우, 이 저작물에 적용된 이용허락조건을 명확하게 나타내어야 합니다.
- 저작권자로부터 별도의 허가를 받으면 이러한 조건들은 적용되지 않습니다.

저작권법에 따른 이용자의 권리는 위의 내용에 의하여 영향을 받지 않습니다.

이것은 [이용허락규약\(Legal Code\)](#)을 이해하기 쉽게 요약한 것입니다.

[Disclaimer](#)

Ph.D Dissertation

박사 학위논문

# Optimization Algorithms for Integrating Advanced Facility-Level Healthcare Technologies into Personal Healthcare Devices

DaeHan Ahn(안 대 한 安大韓)

Department of  
Information and Communication Engineering

DGIST

2018

Ph.D Dissertation

박사 학위논문

# Optimization Algorithms for Integrating Advanced Facility-Level Healthcare Technologies into Personal Healthcare Devices

DaeHan Ahn(안 대 한 安大韓)

Department of  
Information and Communication Engineering

DGIST

2018

# Optimization Algorithms for Integrating Advanced Facility-Level Healthcare Technologies into Personal Healthcare Devices

Advisor: Professor Yongsoon Eun

Co-advisor: Professor Taejoon Park

By

DaeHan Ahn

Department of Information and Communication Engineering

DGIST

A dissertation submitted to the faculty of DGIST in partial fulfillment of the requirements for the degree of Doctor of Philosophy in the Department of Information and Communication Engineering. The study was conducted in accordance with Code of Research Ethics<sup>1</sup>

12. 19. 2017

Approved by

Professor Yongsoon Eun

(Advisor)

\_\_\_\_\_

Professor Taejoon Park

(Co-Advisor)

\_\_\_\_\_

---

<sup>1</sup> Declaration of Ethical Conduct in Research: I, as a graduate student of DGIST, hereby declare that I have not committed any acts that may damage the credibility of my research. These include, but are not limited to: falsification, thesis written by someone else, distortion of research findings or plagiarism. I affirm that my thesis contains honest conclusions based on my own careful research under the guidance of my thesis advisor.

# Optimization Algorithms for Integrating Advanced Facility-Level Healthcare Technologies into Personal Healthcare Devices

DaeHan Ahn

Accepted in partial fulfillment of the requirements for the degree of  
Doctor of Philosophy.

12. 01. 2017

Head of Committee	_____
	Prof. Jihwan P. Choi
Committee Member	_____
	Prof. Yongsoon Eun
Committee Member	_____
	Prof. Taejoon Park
Committee Member	_____
	Prof. Haengju Lee
Committee Member	_____
	Prof. Youngmi Baek

Ph.D/IC  
201322009

안 대 한. DaeHan Ahn. Optimization Algorithms for Integrating Advanced Healthcare Technology in Facility-Level Healthcare Technologies into Personal Healthcare Devices. Department of Information and Communication Engineering. 2018. 89p. Advisors Prof. Yongsoon Eun, Co-Advisors Prof. Taejoon Park.

## ABSTRACT

Healthcare is one of the most important services to preserve the quality of our daily lives, and it is capable of dealing with issues such as global aging, increase in the healthcare cost, and changes to the medical paradigm, i.e., from the in-facility cure to the prevention and cure outside the facility. Accordingly, there has been growing interest in the smart and personalized healthcare systems to diagnose and care themselves. Such systems are capable of providing facility-level diagnosis services by using smart devices (e.g., smartphones, smart watches, and smart glasses). However, in realizing the smart healthcare systems, it is very difficult, albeit impossible, to directly integrate high-precision healthcare technologies or scientific theories into the smart devices due to the stringent limitations in the computing power and battery lifetime, as well as environmental constraints. In this dissertation, we propose three optimization methods in the field of cell counting systems and gait-aid systems for Parkinson's disease patients that address the problems that arise when integrating a specialized healthcare system used in the facilities into mobile or wearable devices. First, we present an optimized cell counting algorithm based on heuristic optimization, which is a key building block for realizing the mobile point-of-care platforms. Second, we develop a learning-based cell counting algorithm that guarantees high performance and efficiency despite the existence of blurry cells due to out-focus and varying brightness of background caused by the limitation of lenses free in-line holographic

apparatus. Finally, we propose smart gait-aid glasses for Parkinson's disease patients based on mathematical optimization.

**Keywords:** Optimization, Smart Healthcare, Cell Counting, Parkinson's Disease, System Integration.

## List of contents

	Page
List of tables.....	iii
List of figures.....	iv~vii
 I. Introduction .....	 1~8
1.1 Global Healthcare Trends .....	1
1.2 Smart Healthcare System.....	2
1.3 Benefits of Smart Healthcare System .....	3
1.4 Challenges of Smart Healthcare.....	4
1.5 Optimization .....	6
1.6 Aims of the Dissertation .....	7
1.7 Dissertation Organization .....	8
 II. Optimization of a cell counting algorithm for mobile point-of-care testing platforms .....	 9~32
2.1 Introduction.....	9
2.2 Materials and Methods.....	13
2.2.1 Experimental Setup.....	13
2.2.2 Overview of Cell Counting .....	16
2.2.3 Cell Library Optimization.....	18
2.2.4 NCC Approximation.....	20
2.3 Results.....	21
2.3.1 Cell Library Optimization.....	21
2.3.2 NCC Approximation.....	23
2.3.3 Measurement Using an Android Device.....	28
2.4 Summary .....	32
 III. Human-level Blood Cell Counting System using NCC-Deep learning algorithm on Lens-free Shadow Image.....	 33~51
3.1 Introduction.....	33



3.2 Cell Counting Architecture .....	36
3.3 Methods.....	37
3.3.1 Candidate Point Selection based on NCC.....	37
3.3.2 Reliable Cell Counting using CNN.....	40
3.4 Results.....	43
3.4.1 Subjects .....	43
3.4.2 Evaluation for the cropped cell image .....	44
3.4.3 Evaluation on the blood sample image .....	46
3.4.4 Elapsed-time evaluation.....	50
3.5 Summary .....	50
IV. Smart Gait-Aid Glasses for Parkinson’s Disease Patients.....	52~73
4.1 Introduction.....	52
4.2 Related Works.....	54
4.2.1 Existing FOG Detection Methods.....	54
4.2.2 Existing Gait-Aid Systems.....	56
4.3 Methods.....	57
4.3.1 Movement Recognition.....	59
4.3.2 FOG Detection On Glasses .....	62
4.3.3 Generation of Visual Patterns .....	66
4.4 Experiments .....	67
4.5 Results.....	69
4.5.1 FOG Detection Performance.....	69
4.5.2 Gait-Aid Performance .....	71
4.5.3 Discussion .....	72
4.6 Summary .....	73
V. Conclusion .....	75~76
Reference .....	77~ 88
요약문.....	89

## List of tables

Table 1. Four heuristic patterns for NCC approximation, judiciously chosen to maximize the detection probability for a cell, as well as to reduce the runtime as much as possible. Employing Patterns 1, 2 and 3 reduces the runtime for evaluating NCC values by 50% ~ 75% at the expense of some accuracy loss (1.4% ~ 6.1%). Patterns 1 and 2 yield the highest detection probability (97.1% ~ 98.6%) and maintain the same amount of runtime reduction (50% ). Pattern 3 achieves further reduction in runtime (75%) compared to Patterns 1 and 2, but its detection probability becomes lower (93.9%). Pattern 4 has the poorest detection probability (50.1%) and, hence, may not meet the accuracy requirement. ....	24
Table 2. The list of subjects to compare with the proposed algorithm. That consists of 9 algorithms based the three base types .....	43
Table 3. The evaluation result of each algorithms on the blood sample image.....	48
Table 4. PD patients for preliminary experiments having a disease duration of 6.80 years, H-Y (Hoehn and Yahr) scale of 2.55, and UPDRS (Unified Parkinson's Disease Rating Scale scored by clinician) III score of 30.00 on average .....	67
Table 5. The cueing effects of simplified and proposed scenarios on PD patients; compared with the baseline, the proposed scenario improves the average number of steps, velocity and stride length by 22.6%, 37.2% and 31.7%, respectively .....	71

## List of figures

- Figure 1. The concept of the optimization algorithm to connect facility healthcare and the personal healthcare system in our daily life..... 7
- Figure 2. Schematic figure of an affordable point-of-care (POC) testing platform based on a commercially available smart phone, which can be integrated with a microfluidic system and an automated cell counting program. (a) The POC testing platform is composed of a smart phone CMOS sensor, a microfluidic chip and a chip cover (not yet available) containing an active mirror; it can simply be assembled with a commercially available smart phone by using a chip cover assay. The microfluidic chip is inserted into the cover assay and the CMOS sensor can take images with no optical lens... ..... 10
- Figure 3. The cell imaging apparatus connected to an Android mobile device. The imaging apparatus is designed with an automated microfluidic chip alignment system, a syringe pump, a halogen lamp and a CCD imaging platform, while the Android device has a computing capability comparable to that of an Intel Atom processor, which is far slower than the typical processors for desktop platforms. .... 15
- Figure 4. Cell library optimization to avoid inefficiency caused by random construction of the library. (a) The influence (%) indicates the proportion of the cell count of each cell image to the total counting result, which varies significantly from one cell image to another; some cell images cannot find any cells, because all of the cells found by these cell images are already counted by other duplicated and/or similar cell images. (b) This loss can further be compensated for by reducing the threshold value, e.g., 24 cells are marked under a high threshold value of 0.67, while 42 cells are identified after decreasing the threshold to 0.60, where the latter is close to the result of manual counting. (c) A receiver operating characteristic (ROC) curve plots a true positive rate (i.e., the ratio of the count of correct cell detection to the total cell count) vs. a false positive rate (i.e., the ratio of the count of false cell detection to the total cell count)

by varying the threshold value from 0.60 to 0.67. As shown in the ROC curve, the algorithm becomes less sensitive as the threshold value gets higher, thus resulting in the decreased count of cells. (d) The number of counted cells linearly depends on, or is inversely proportional to, the threshold value; decreasing the threshold value increases the number of counted cells. This relationship can be used to adjust the threshold value to counter the loss in counting accuracy after optimizing the library. .... 19

Figure 5. The Bland-Altman plot, evaluating the accuracy of the optimized cell counting algorithm in comparison with an original algorithm. The x-axis is the average of counting results of original and optimized algorithms, while the y-axis is the difference between them. It has a bias of 46.56 cells, and upper and lower limits of 201.72 and -108.60, respectively. .... 25

Figure 6. The difference in counted cells between the original algorithm and the algorithm with NCC approximation (heuristic Patterns 1~4). The closer the difference is to zero, the more accurate the algorithm with NCC approximation gets. Since all four heuristic patterns for NCC approximation cross zero, it is possible to find the best threshold values that can practically eliminate the accuracy loss, which are 0.615, 0.617, 0.583 and 0.498 for heuristic Patterns 1, 2, 3 and 4, respectively. The heuristic patterns 1 and 2 satisfy the accuracy requirement (i.e., zero loss) for the range of threshold (>0.6) and reduces the runtime required for NCC by 50%. .... 27

Figure 7. Evaluation of the counting accuracy of the original and optimized algorithms. (a) For each of six channels, 10 count results of the original algorithm, each with its own randomly-selected cell image library, are plotted based on the distance (up to 30 mm) from the inlet port of each channel; the count result of the original algorithm that yields the best match with manual counting is plotted, as well. In the original algorithm (using 150 random cell images), the number of counted cells varies a lot (up to 30%), due to the random generation of cell image library for each execution. (b) The counting results of the original algorithm (best configuration) and the optimized algorithm (via cross-validation) are compared. For each of the channels, a specific cell image

library for the optimized algorithm is generated by using the rest of five channel images to conduct cross-validation. The optimized algorithm exhibits an average difference of 5.05%. This demonstrates the robustness and effectiveness of the proposed approach. ....	29
Figure 8. Comparison with manual counting and another cell counting algorithm [34]. With normal blood sample images, all three methods have the same results. For noisy images with intensity variations, NCC-based algorithms (both original and optimized) produce counting results close to those of manual counting, while [34] fails to reliably count cells.....	30
Figure 9. The runtime of the original algorithm and the optimized algorithms employing either or both of an optimized cell library to minimize the number of cell images and heuristic Pattern 1 to skip NCC computations for some points. The runtime of the original algorithm that evaluates NCC values for each and every point is, on average, 740.42 s, while that of the optimized algorithm is only 64.12 s, achieving almost a 11.5× runtime reduction with accuracy loss less than 1%. The result also demonstrates that the cell library optimization reduces the runtime by 86.6% (from 740.42 s to 99.52 s), while heuristic Pattern 1 contributes to a 50.1% runtime reduction (from 529.5 s to 264 s).....	31
Figure 10. Schematic of introduction for the NCC-CNN algorithm .....	36
Figure 11. Schematic print of the in-line holographic apparatus and the cause of the blurry cell image .....	38
Figure 12. Intensity and correlation coefficient of normal, blurry cell and background noise .....	39
Figure 13. CNN architecture. That consists of three hidden layers with two ReLU function, a max pooling layer, fully connected layer and softmax logistic regression .....	41
Figure 14. Demonstration of NCC-CNN process .....	42
Figure 15. The sample images of the normal cell, blurry cell and background.....	44
Figure 16. The performance of each algorithm while increasing the number of training dataset. a) is for normal cell image and b) is for blurry cell image .....	46

Figure 17. The original image, manual cell counting result and the demonstration of each algorithm.....	47
Figure 18. The elapsed-time of each algorithm .....	49
Figure 19. Smart gait-aid system consisting of freezing of gait (FOG) detection and movement recognition subsystems. ....	58
Figure 20. (a) Sensor coordinates (3D) where the z-axis is the wearer's gaze direction; (b) sensor and global coordinates (2D) with respect to the gaze and walking direction, respectively; and (c) walking distance estimation that transforms sensor readings from into global coordinates. ....	59
Figure 21. (a) Definition of step length; (b) step length vs. head moving distance (HMD) .....	61
Figure 22. Measured step length (obtained by using a system [48]) and HMD before FOG episodes.....	63
Figure 23. FOG detection process of FOGDOG: it first computes the walking distance, $D_t$ from sensor reading in the sliding time window; estimates the two distance values, $D_t^{ref}$ and $D_t'$ , as well as the number of steps, $N_t^{step}$ by analyzing the partition of $D_t$ ; and finally computes $FOGDOG_t$ .....	65
Figure 24. Visual cues when the downward gaze angle is equal to (a) $45^\circ$ and (b) $90^\circ$ . The proposed system projects virtual cues consistently with the physical cues in the real world .....	66
Figure 25. FOG detection of three methods over time: FI, FOGC and FOGDOG achieve 78.57%, 84.52% and 92.86% accuracy, respectively .....	69
Figure 26. FOG detection of three methods using: (a) sensitivity, (b) specificity, and (c) F1 scores. FOGDOG outperforms FI and FOGC by 9~18% and 5~11%, respectively .....	70

# **I. Introduction**

## **1.1 Global Healthcare Trends**

In recent years, there has been an increasing demand for global healthcare to address problems associated with increasing medical costs and aging of the global population, as well as meet the needs for improving the quality of life. In 2016, the United States spent more than 15% of its gross domestic product (GDP) on healthcare, amounting to more than \$ 20,000 per family [1]. According to a report [2], the healthcare market will increase from \$ 2 million in 2016 to \$ 97 million by 2021. Globally, healthcare spends are projected to reach \$ 8.7 trillion by 2020, and the percentage of GDP spent on healthcare is estimated to 10.5% in 2020 [3]. In particular, smart healthcare that integrates internet of things (IoT) technology into healthcare gives a huge impact on the healthcare market. According to a report in [4], the smart healthcare market is expected to register a compound annual growth rate (CAGR) of 24.5% between 2016 and 2020 because, depending on the emergence of IoT device, the paradigm of healthcare will be changed from the way it is treated at the facility to the way it is treated and prevented at anytime and anywhere. Along with this trend, the healthcare industry is quickly shifting to the self-diagnosing age possibly by using wearable device as the next step in healthcare. For instance, there are an increasing number of wearable devices that can monitor heart rates, respiratory rates, oxygen levels and blood pressure, temperature, activities and sleep patterns. Such devices can, when needed, alert the wearer, predict the risks, and suggest interventions to avoid becoming the disease in the future. Moreover, they are able to record health information on a scale that was never before possible, and such data will give us right insight in improving the quality of life and advancing the technology in the next decade.

## 1.2 Smart Healthcare Systems

Smart healthcare system can be realized by using different biometric sensors that capture the human's bio-signals [5]. Such systems analyze these signals via algorithms to produce readings on an application to provide high-quality healthcare services. Typically, wearable devices such as smart watches and smart glasses are used for the smart healthcare. In the last decade, many manufacturers provided various products. SAMSUNG and APPLE released smart watches to measure and record blood pressure, health conditions [6] [7], and NIKE and ADIDAS released smart wristbands to record user's exercises [8] [9]. In addition, there are smart shoes and rings [10] [11]. These devices are capable of playing important roles for the smart healthcare as they can read user's bio-signals by using the embedded sensors and save them in the storage after data processing.

The representative sensors for recording bio-signal are as follows.

- **Inertial Measurement Unit (IMU):** it is typically used to analyze the body's movement, and consists of accelerometer, gyroscope and magnetometer that measure a body's acceleration, angular rate, and the magnetic field surrounding the body, respectively.
- **Heart Rate Sensor:** it allows to measure a wearer's heart rate in real-time and helps to diagnose the wearer's serious condition such as heart attack.
- **Global Positioning System (GPS):** it provides the wearer's position in the world, and it used to provide the location and distance.

In general, different sensors produce different types of measurements, but it is possible that the same sensor can be used in many different ways. For example, a 3-axis accelerometer of IMU measures movements in every direction. The data gathered by the



accelerometer can be converted into the number of steps, distance, the burned calories and other measurements about the activities. Thus, the way of the interpreting of the data is important.

### 1.3 Benefits of Smart Healthcare System

There is no doubt that smart healthcare systems are transforming how the existing healthcare systems deliver the healthcare solutions. That is, the IoT technology is constantly providing new apps and devices as well as integrated healthcare systems for smart healthcare. Thus, it gives multiple opportunities and benefits to physician, patient and public.

For the physician [12]:

- **Financial benefits:** smart healthcare service can improve more than 50% of healthcare costs by saving time and reducing efforts.
- **Lower cases of malpractice claims:** it shares the experience about the inappropriate treatment between doctors, and give the doctor a full history of a disease. In reality, after starting the smart healthcare service, the number of malpractice claims dropped by 96%.
- **Faster lap results:** most smart healthcare system shows the analyzed result in the real-time. Also, that connects to the server in a facility, and can use the high-quality service in the point-of-care.
- **Faster turnaround:** facility using smart healthcare service reduce the auditing time from 3.9 to 1.4 hours

- **Operational efficiency:** physician can access to the right equipment and medication when they needed at the right time.
- **Time savings:** over 80% of healthcare expert claimed that the smart healthcare service reduces time to diagnosis

For the patient and public:

- **Ease of access:** by using a mobile and wearable device that can be easily accessed and be used, one who want to be treated can access directly the experts anywhere and anytime.
- **Ease of use:** most smart healthcare system provides the user interface through the application for user convenient.
- **improved care** - smart healthcare connects between a facility and a patient or public. Thus, a patient and public can give and get the suitable information from the skilled workforce whenever they need it.
- **Reduced cost and time** – smart healthcare system provides point-of-care testing in the real time. Thus, one using the system do not need to visit the hospital frequently.

#### 1.4 Challenges of Smart Healthcare

In 2015, more than 165,000 applications related to smart healthcare were reported on the application market. That is more than doubling over the past years. Among the applications, while the application related to wellness management, such as fitness, stress and diet takes more than 80%, there are few services and application related to diagnosis

and prevention of diseases [13]. One of the critical reasons for that is the technology gap between the advanced technology and technical and environmental resource available in a user's daily life. Therefore, there are some problems in applying the advanced technology to the daily life: 1) Most healthcare equipment used to demonstrate the advanced technology has a high-performance processor, expensive cost, heavy size that the user cannot carry. Also, most people do not want to pay for taking the equipment; 2) The mobile and wearable device available in the daily life does not guarantee the high performance as much as the equipment in the facility since the devices do not have the high resolution and sensitive sensors as well as the facility's equipment; and 3) In some cases, real-time processing is difficult due to the limitation of the mobile and wearable device's computing power. Because of these problems, many companies are investing a lot of development time to figure out how people can use even if they find the advance technology [14].

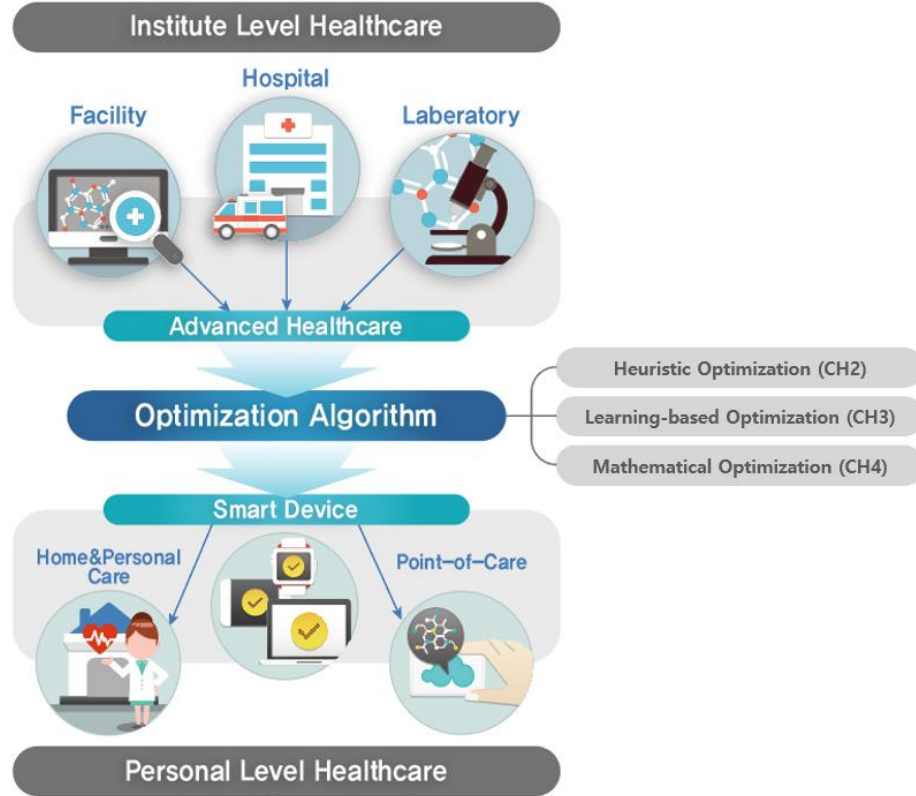
To tackle the above-mentioned barriers, the following challenges must be solved: 1) Using the smart device such as smartphone, wearable device since any user can easily access to smart device; 2) developing and improving sensor or processor that runs on the smart device while maintaining or improving the performance of the existing technologies, but it is impossible in the short term; and 3) improving the existing algorithm for use anywhere and anytime. When the algorithm capable of meeting the challenge, and replacing existing expensive equipment is developed, that can dramatically increase application range.

## 1.5 Optimization

In our daily lives, we often deal with the optimization problems. For example, when we want to buy something, we consider financial condition, the reason for purchase, the quality of after service (AS) and etc., and decide to buy one after comparing between various products. The reason for the considerations is maximizing the effectiveness, minimizing the cost and selecting the optimized option to meet the needs. We call this solution the optimization.

Optimization is to find the act or configuration of obtaining the best result or feasible solution under given constraints, circumstances or the needs of anyone who want to use [15]. Traditionally, optimization problem used the mathematical function by the convex, linear, non-linear and heuristic model. In details, it defines a mathematical function for a physical phenomenon or system operation under a given condition, and then the function adjusts the parameters in a direction close to the desire value, and finds the optimum value. To achieve that, various solutions have been proposed such as first/second order differential, line search, trust region.

In the system engineering fields, the optimization can be defined as the design of the algorithm or system to achieve some goals based on the existing knowledge, system or algorithm [16]. There are various optimization methods. For example, system optimization enhances the system capabilities by improving and integrating subsystem elements. algorithmic optimization is finding the minimum values of the mathematical functions by evaluating the design tradeoffs depending on algorithmic options. To support the methods, various algorithms are proposed such as genetic algorithm, dynamic programming, simulated annealing.



**Figure 1** the concept of the optimization algorithm for integrating facility-level healthcare into the personal healthcare system in our daily life.

As the result of that, The optimization has the benefits such as improving the performance, minimizing the errors, overcoming the environmental and hardware constraints. Thus, it plays the critical role to integrate the advanced technology into the smart systems or devices in our daily life.

## 1.6 Aims of the Dissertation

In this dissertation, we represent the optimization algorithms to transfer the advanced healthcare system of the facility level to the personal level healthcare system used in our daily life. Figure 1 shows the concept of the optimization algorithm to connect facility-level healthcare and the personal healthcare system in our daily life. To achieve the goal,

we define the three optimization methods: 1) Heuristic optimization. This is the optimization method that improves a system by applying the experience and expertise of a physician, expert, patient, and normal people.; 2) Learning-based optimization. This is the way to maximize the performance and to reduce the complexity of the system based on a machine learning algorithm.; and 3) Mathematical optimization. This redefines or customizes the existing scientific knowledge or formulas for applying the specific environments. Through the dissertation, we present the two major concerns that is a cell counting system and gait-aid system for Parkinson's disease, and three chapters that illustrate the optimized system using these optimization methods. In summary, first, cell counting system. In the past, the system was used in the facility level. But it is needed in the Point-Of-Care Testing (POCT) more than in the facility. To apply the system to POCT, it is needed a) how can the system in the facility apply to the mobile device for POCT. To solve that, we propose a heuristic optimization. b) how to maximize the performance. To achieve that, we designed a system using learning-based optimization. Second, we considered the gait-aid system of Parkinson's disease, and found the more efficient method for the gait-aid system based on the mathematical optimization.

## **1.7 Dissertation Organization**

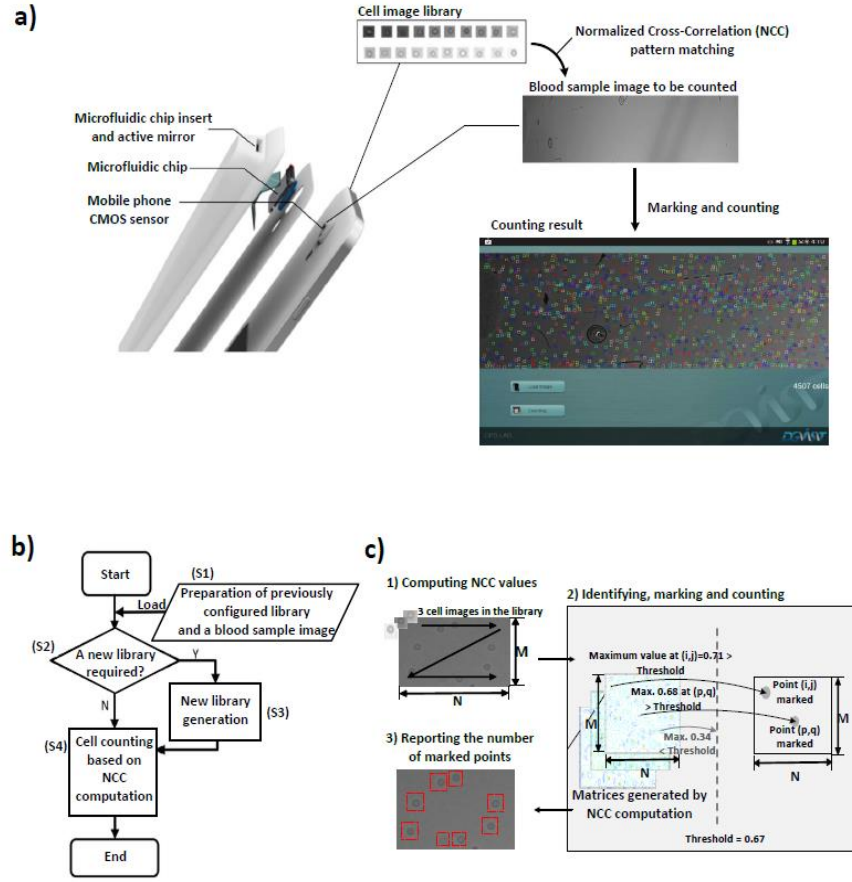
The remainder of this dissertation is organized as follows. Chapter 2 discusses the optimization of cell counting algorithm for mobile point-of-care testing platform. Chapter 3 discusses human-level blood cell counting system using learning-based optimization. Chapter 4 discusses mathematical optimization for application of people with Parkinson's disease. Finally, the dissertation concludes chapter 6.

## **II. Optimization of a cell counting algorithm for mobile point-of-care testing platforms**

### **2.1 Introduction**

Human immunodeficiency virus (HIV) remains one of the most fatal and infectious viruses. Due to inadequate accesses to HIV prevention and treatment methods, HIV infection has rapidly spread in developing countries. Consequently, an estimated 35.3 million people worldwide were living with HIV in 2012 [17]. As one of diagnosis and care methods for such a disease, point-of-care (POC) testing can generate results quicker and, hence, can start the treatment much sooner than laboratory-based testing methods [18]. In particular, counting the number of specific cells in a blood sample is one of the most important tests in various biological and medical fields [19] [20] [21] [22]; e.g., HIV testing exploits the fact that HIV-infected individuals have CD4+ T lymphocyte counts below 350 cells per microliter of blood [19].

There are manual and automatic methods for counting specific cells. The manual cell counting method is the most time-consuming and the most labor-intensive approach [23] [24] [25], which means it is not suitable for POC testing in a rapid, consistent and repeated manner [18]. Due to such limitations, many researchers have studied various automatic cell counting methods based on hardware approaches, such as electrical impedance measurement [26] [27], optical inspection [28] [29] or image processing [18] [30] [31]. The electrical impedance measurement method is a hardware-based technique that translates the change of impedance into a count of cells when particles pass through a small aperture. The optical inspection method is also a hardware-based technique that uses laser



**Figure 2.** Schematic figure of an affordable point-of-care (POC) testing platform based on a commercially available smart phone, which can be integrated with a microfluidic system and an automated cell counting program. (a) The POC testing platform is composed of a smart phone CMOS sensor, a microfluidic chip and a chip cover (not yet available) containing an active mirror; it can simply be assembled with a commercially available smart phone by using a chip cover assay. The microfluidic chip is inserted into the cover assay and the CMOS sensor can take images with no optical lens. Note that actual cell images were captured using the apparatus in Figure 2. (b) The lensless image generated by an in-line holographic technique can be processed based on an Android smart phone, i.e., a cell (shadow) image is counted by an automated cell counting program that consists of four steps: (S1) preparing a blood sample image captured by the imaging apparatus, as well as a pre-configured cell image library; (S2) checking whether or not a new cell image library is required for the captured image; (S3) generating a new cell image library if required; (S4) computing normalized cross-correlation (NCC) values for the entire image followed by identifying, marking and counting cells. (c) The actual counting process in (S4) first computes NCC values for the entire blood sample image by applying each and every cell image in the library in a zig-zag manner; then marking and counting point  $(i, j)$  as a cell if the maximum of NCC values for  $(i, j)$  exceeds a threshold, e.g., 0.67; and finally, reporting the number of marked points as counted cells.



light to identify and count cells. However, both methods, which similarly exploit the physical properties of cells, are expensive. Instead of relying on either manual inspection or costly hardware, software-based image processing approaches with inexpensive hardware, such as automated imaging cytometry and calculus-based cell counting [25] [26], can be adopted as a cost-effective POC testing method. This is because such a cell counting method can be far faster and more accurate than the manual approach, while it is much cheaper than the aforementioned hardware approaches. For instance, a recently proposed approach [18] can count cells 5760x faster than the manual method at practically no equipment cost; it achieves this high performance by computing normalized cross-correlation (NCC) values between two images, i.e., a blood sample image and a cell image in the library, to quantify the similarity between the two images. Such an approach for counting cells gives a few advantages over other methods, such as automated imaging cytometry; NCC computation is much faster and more accurate than other approaches, because it effectively utilizes the shape of a certain cell to locate and count cells.

The accessibility of POC tests has significantly expanded in both developed and developing countries [23] [32]. However, hardware-based cell counting approaches have not been widely accepted yet, due to the high cost of procuring the necessary equipment and training the technicians for such sophisticated equipment [33]. On the other hand, mobile POC testing [33] [34], which automates disease diagnosis using mobile devices such as smart phones and tablets, has emerged as an attractive alternative, as mobile devices become more affordable, portable and powerful. For example, Zhu et al. [34] presented a cost-effective imaging cytometry platform and custom-developed software for mobile POC testing. The schematic in Figure 2a shows how a commercially available smart

phone running an automated cell counting algorithm can be used as an affordable POC testing device if integrated with a microfluidic platform in the form of a cover assay.

Despite such benefits, however, we note that mobile devices with a small form factor are still not suitable for the software-based methods. This is because such an algorithm often demands considerable computing capability to reliably deal with image anomalies, e.g., variations in background intensity, brightness and noise, while mobile devices with a small form factor have limited computing capability and battery capacity. For example, it takes more than 10 minutes for the algorithm running on an Android smart phone to count cells in a blood sample image. Therefore, it is crucial to optimize such a software-based approach for mobile devices with a small form factor to provide quick and uninterrupted services for an extended period of time.

In this chapter, we propose two synergistic optimization techniques for the software-based algorithm based on NCC, such that it is suitable for Android smart phones after identifying the sources of its inefficiency. First, we observe that evaluating the NCC values for each point of a blood sample image with each and every cell image in the library is responsible for most of the runtime and energy consumption, both of which are proportional to the product of the number of cell images in the library and the number of points in the blood sample image. Second, we note that some cell images in the library are similar or duplicated because cell images are manually and randomly chosen. Meanwhile, these similar or duplicated cell images just increase the runtime and energy consumption without notably contributing to higher counting accuracy. Hereafter, we use runtime and energy consumption interchangeably, because they are proportional to each other. Third, a cell often spans across multiple points in a blood sample image, while evaluating NCC

values for all of the points in the vicinity of a cell leads to detection of only a single cell. Thus, we note that evaluating NCC values for all of the points is highly redundant.

Motivated by these three observations, we propose the following two optimization techniques. First, we develop a technique to systematically remove duplicated or similar cell images from the library by evaluating the influence or loss of each cell image on the counting accuracy when removed. Second, we devise heuristic patterns that determine which points for which we skip NCC evaluations. Note that eliminating similar cell images in the library and/or skipping NCC evaluations for some points can decrease NCC values for points where cells are located. Meanwhile, these NCC values are compared against a threshold value to determine whether or not a cell exists in the point in a blood sample image. Consequently, the decreased NCC values for these points can incur some loss of counting accuracy. To compensate for the accuracy loss, we also propose to adjust the threshold value such that the degradation of counting accuracy is minimized.

We implement the optimized cell counting algorithm in an Android smart phone and evaluate its runtime. The evaluation result demonstrates that the system adopting the proposed optimized algorithm outperforms the original algorithm, reducing the runtime by 11.5 $\times$ . Accordingly, our work enables scalable solutions for realizing disposable low-cost POC testing platforms based on inexpensive mobile devices, thus offering quick blood tests for the diagnoses of diseases plaguing many developing countries.

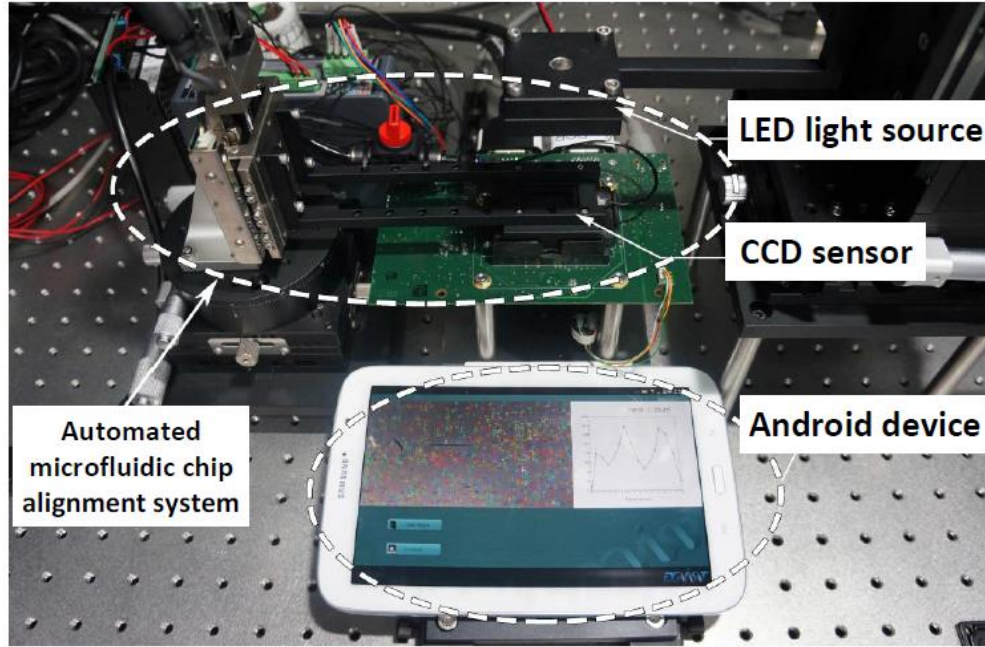
## **2.2 Materials and Methods**

### **2.2.1 Experimental Setup**

An Android smart phone is connected to an imaging apparatus shown in Figure 3 to

capture  $3334 \times 445$  blood sample images. The thus obtained images are used throughout the method development and validation. The specification of the smart phone is as follows: A 1.6-GHz quad-core CPU, a 533-MHz GPU, and 2-GB RAM running Android 4.1.2. Note that its computing capability is comparable to that of an Intel Atom processor, which is far slower than typical processors used for the desktop platform.

The imaging apparatus is designed for in-line holographic cell images on a microfluidic channel surface. The apparatus is designed with an automated microfluidic chip alignment system (cRIO, NI Korea, Korea), a syringe pump (Fusion 100 Touch, Revodix, Korea), a halogen lamp (FOK-100W, Micro-Lite, Korea) and a CCD imaging platform (Foveon F13 AVF-36A Development Kit, Alternative Vision Corporation, Tucson, AZ). Chip alignment with 10  $\mu$ m resolution is achieved with a precise manual  $xy$  stage (TPS-1, NAMIL Optical Co., Korea). To magnify in-line holographic cell images of targeted cells by  $1.5 \times$  magnification, the gap between the bottom of the microfluidic chip and the top surface of the CCD image sensor (Fx17-78-F13D-07v, Foveon Inc., USA) is determined as 1.1 mm. The halogen lamp, as a white light source, emits through a fifty-micron pin hole (#56282, Edmund Optics, Korea). The in-line holographic cell patterns are directly imaged on the CCD image sensor without a lens, where the CCD sensor features



**Figure 3.** The cell imaging apparatus connected to an Android mobile device. The imaging apparatus is designed with an automated microfluidic chip alignment system, a syringe pump, a halogen lamp and a CCD imaging platform, while the Android device has a computing capability comparable to that of an Intel Atom processor, which is far slower than the typical processors for desktop platforms.

more than 14 million square pixels ( $7.8\ \mu\text{m}$ , pixel pitch) across the active sensor array area ( $24.9\ \text{mm}$ , effective diagonal dimension) where the Foveon color CCD chip enables imaging with microscope cover slides ( $24\ \text{mm} \times 32\ \text{mm} \times 0.10\ \text{mm}$ , Knittel Glaser, Germany).

As detailed in [18], NIH3T3 cells (mouse fibroblast cell line, CRL-1658) are cultured in Dulbecco's modified Eagle medium with high glucose (DMEM) containing 10% FBS, 100 U/mL penicillin, 100 g/mL streptomycin, and 2 mM L-glutamine. The NIH3T3 cells are maintained in the complete cell medium and grown at  $37^{\circ}\text{C}$  in a humidified 5%  $\text{CO}_2$  environment.

After the cell culture process, a suspension of the NIH3T3 cells is injected

(approximately 200  $\mu\text{L}$  total volume) into the microfluidic channel with a flow rate of 0.05  $\mu\text{L}/\text{h}$ . The controlled velocity of the cell containing fluid is generated by the automated syringe pump. The NIH3T3 cells refer to the targeted cells of the automatic cell counting sink and attach to the bottom of the microfluidic channel surface.

To obtain blood and cultured cell smears for imaging experiments, blood is first collected by pricking the finger with a needle. A small drop of blood sample is then dropped on the top of a slide glass. Tilting the cover slip at a  $30^\circ$  angle allows blood to spread across the edge. Thereafter, smoothly and quickly pulling the slide glass forward allows the drop of blood to spread even more thinly onto the slide. Next, the blood-stained slide glass is dried at room temperature for about 1 minute. Afterwards, the smeared blood film is dropped into 70% methanol and air-dried again before staining it by the Wright–Giemsa staining kit (Sigma-Aldrich Inc., St. Louis, MO, USA). The dried blood film is then placed into Coplin jars (5-PC glass staining jar, Citotest Labware Manufacturing Co., LTD., China), which contain approximately 50 mL Wright-Giemsa stain solution, for 30 seconds. Finally, the slide is removed from the stain and placed into de-ionized water or phosphate buffer solution (pH 7.2) for approximately 10 minutes and air-dried. This process allows the blood and cultured cell samples to be ready to be observed under the cell imaging apparatus.

### **2.2.2 Overview of Cell Counting**

The cell counting algorithm based on NCC generally consists of four steps, as shown in Figure 2b: (S1) preparing a blood sample image captured by the imaging apparatus, as well as a pre-configured cell image library; (S2) checking whether or not a new cell image library is required for the captured image; (S3) generating a new cell image library if

required; (S4) computing NCC values for the entire image followed by identifying, marking and counting cells. According to [18], if a generated library already exists (S2), there is no need to create another library (S3); otherwise, the cell library images must be manually predefined by marking cells located in random sections of the blood sample image (S3).

Computing NCC values allows us to identify cell locations in a blood sample image captured by any cell imaging apparatus [18] [35]. Counting cells is essentially a process of searching for the similarity between the blood sample image and cell images from the library; since both of the images are from the same apparatus, it is capable of accurately locating all cells of a similar shape, thus reliably counting the number of cells.  $R(i, j)$ , which denotes the NCC value at point  $(i, j)$  in a blood sample image, ranges from -1.0 to +1.0 and is calculated by:

$$R(i, j) = \frac{\sum_{y=0}^{L-1} \sum_{x=0}^{K-1} (\omega(x, y) - \bar{\omega})(f(x+i, y+j) - \bar{f}(i, j))}{\sqrt{\sum_{y=0}^{L-1} \sum_{x=0}^{K-1} (\omega(x, y) - \bar{\omega})^2} \sqrt{\sum_{y=0}^{L-1} \sum_{x=0}^{K-1} (f(x+i, y+j) - \bar{f}(i, j))^2}} \quad (1)$$

where  $0 \leq i \leq M - K$  and  $0 \leq j \leq N - L$ ,  $\omega(x, y)$ ,  $f(x, y)$ ,  $\bar{\omega}$  and  $\bar{f}$  denote a cell image of  $K \times L$  pixel points from the library, a blood sample image of  $M \times N$  pixel points (e.g.,  $3,334 \times 445$  pixel points in our implementation), a mean of  $\omega(x, y)$  and a mean of a  $K \times L$  sub-image of  $f$  starting at  $(i, j)$ , respectively. The closer  $R(i, j)$  is to -1.0 or +1.0, the stronger the two images are correlated. On the contrary, the two images are highly irrelevant when the value is close to 0.

A threshold value is used to decide whether or not a cell exists at  $(i, j)$ ; if  $R(i, j)$  is higher than the threshold value, the cell counting algorithm marks point  $(i, j)$  as a cell. After computing the NCC values for the entire sample image with each and every cell image in

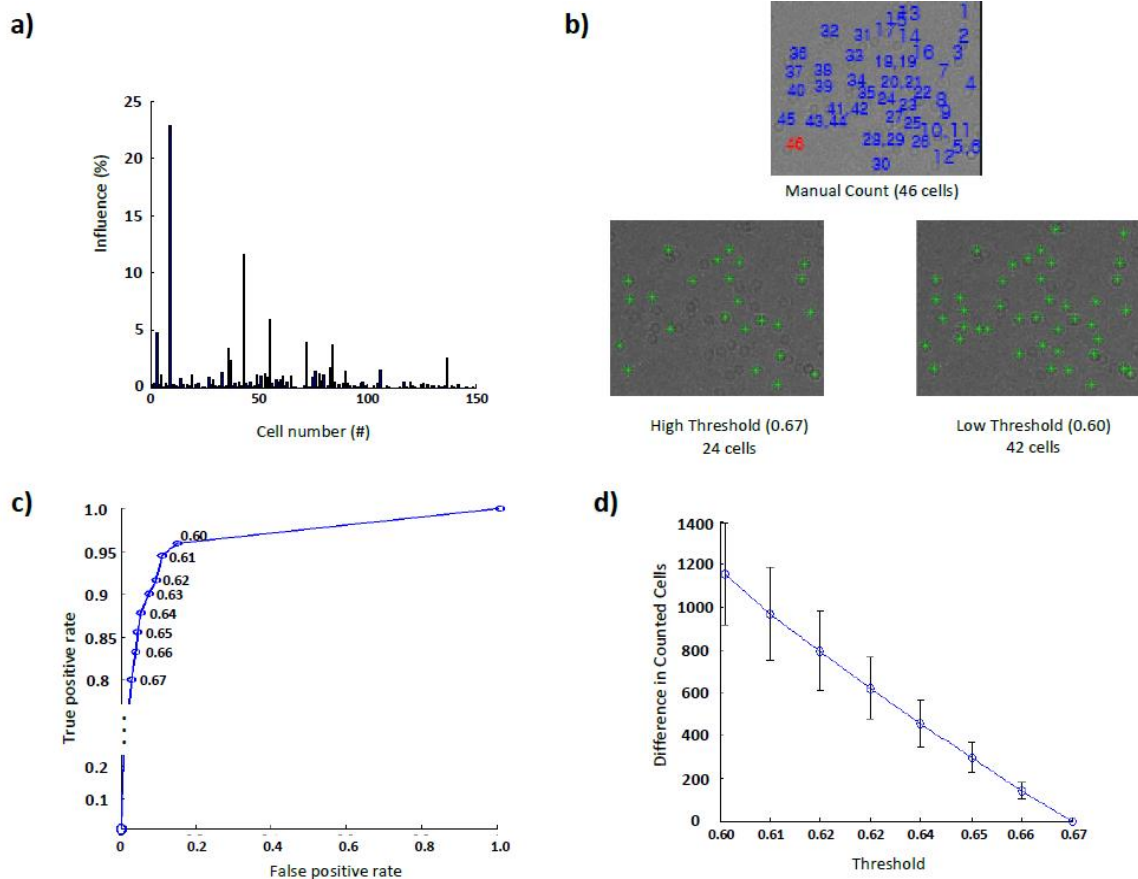
the library, the algorithm counts the number of marked points and reports the number of counted cells as illustrated in Figure 2c. As the threshold value gets lower, the algorithm becomes more sensitive and perceives more cells, thus resulting in an increased count of cells. This indicates that determining an appropriate threshold value directly affects the accuracy of the algorithm. In [18], the threshold value was experimentally determined so as to minimize the difference between automated and manual counting results.

In the original NCC-based counting algorithm, however, we observe considerable inefficiency in Steps (S3) and (S4). First, a naive approach, which randomly chooses cell images to build the cell image library in (S3), often leads to more cell images than needed to achieve the desired accuracy, unnecessarily increasing the runtime proportional to the number of redundant cell images. Second, NCC values are evaluated for each and every point in (S4), while a cell in a blood sample image spans over multiple points. Thus, it is very likely to obtain high NCC values at multiple points in the vicinity of the cell. Since our objective is not to identify the exact center location of each cell, but to count the total number of cells, such multiple NCC evaluations for detecting a single cell are redundant. To avoid such inefficiency, we present two synergistic techniques optimizing the cell image library and approximating NCC evaluations.

### **2.2.3 Cell Library Optimization**

Since the runtime is proportional to the number of cell images in the library, we propose a systematic method that can remove duplicated or similar images from the library without notably impacting the accuracy. This, in turn, reduces the number of cell images in the library and, thus, the runtime. In the original algorithm, 150 cell images were manually identified and randomly selected from various blood sample images to construct





**Figure 4.** Cell library optimization to avoid inefficiency caused by random construction of the library. (a) The influence (%) indicates the proportion of the cell count of each cell image to the total counting result, which varies significantly from one cell image to another; some cell images cannot find any cells, because all of the cells found by these cell images are already counted by other duplicated and/or similar cell images. (b) This loss can further be compensated for by reducing the threshold value, e.g., 24 cells are marked under a high threshold value of 0.67, while 42 cells are identified after decreasing the threshold to 0.60, where the latter is close to the result of manual counting. (c) A receiver operating characteristic (ROC) curve plots a true positive rate (i.e., the ratio of the count of correct cell detection to the total cell count) vs. a false positive rate (i.e., the ratio of the count of false cell detection to the total cell count) by varying the threshold value from 0.60 to 0.67. As shown in the ROC curve, the algorithm becomes less sensitive as the threshold value gets higher, thus resulting in the decreased count of cells. (d) The number of counted cells linearly depends on, or is inversely proportional to, the threshold value; decreasing the threshold value increases the number of counted cells. This relationship can be used to adjust the threshold value to counter the loss in counting accuracy after optimizing the library.

a cell image library. However, we observe that many similar cell images in the library do not significantly contribute to augmenting the counting accuracy, while increasing the runtime. In practice, it is inevitable to have multiple duplicated or similar images under such a random selection strategy. Therefore, we need a systematic method to eliminate those redundant cell images in the library.

To further motivate our proposed approach, we evaluate the influence of each cell image regarding the accuracy by counting the number of cells discovered by a particular cell image in the library, as shown in Figure 4a, where the influence (%) indicates the proportion of the cell count of each cell image to the total counting result. In the library, some cell images cannot find any cells to be counted, because all of the cells, which are found by these cell images, are already counted by other duplicated and/or similar cell images. In the presence of similar cell images, the influence of some cell images in the library on counting accuracy is very small, because most of the cells identified by them are the same. Eliminating these duplicated or similar cell images incurs small loss in cell counting accuracy because cell images in the library can be slightly less similar to the removed cell images, leading to lower NCC values for some cells. However, we observe that such loss can be compensated for by reducing the threshold value. Based on these results, we present a joint optimization approach that: (i) removes images with the least losses from the library; and then (ii) adjusts the threshold to counter these losses.

#### **2.2.4 NCC Approximation**

The integral part of the cell counting algorithm consists of two steps, as illustrated in Figure 2c. First, it identifies the locations of cells by computing NCC values for each point

with each and every cell image in the library; the points with their NCC values higher than the threshold value are identified as cells and are stored in  $(M-K+1) \times (N-L+1)$  matrices, where  $M$  and  $N$  are the number of rows and columns in a blood sample image, while  $K$  and  $L$  indicate the size of a cell library image, as defined in Section 2.2. Second, all of the values in the matrix are read back to mark and count identified cells.

To reduce the runtime, we exploit the fact that a single cell usually appears as a cluster of points in the matrix, where a cluster has a maximum size of  $m \times n$ , e.g.,  $3 \times 3$ , as shown in Figure 4b. Since the cell counting algorithm may recognize a cell if the NCC value for at least one point of the cluster is higher than the threshold value, it is redundant to process each and every point on the blood sample image to evaluate NCC values. Hence, we may get an approximated counting result by skipping NCC evaluations for neighboring points as far as we can mark at least one point for a cell in the  $M \times N$  matrix.

## 2.3 Results

In this section, we evaluate the accuracy and runtime of the cell counting algorithm, employing our proposed optimization techniques using an Android smart phone, and compare them against the original algorithm using the original library containing 150 randomly-selected cell images.

### 2.3.1 Cell Library Optimization

To build an optimized cell image library, we first evaluate the influence of each of the 150 cell images in the library used for our previous study for four different channels of the blood sample image. Figure 4a plots the influence of each cell image in the library on the counting result. We note that the influence of each cell image is almost the same for all

channels, implying that our optimization technique is applicable to the entire blood sample image. Using our proposed optimization technique, we identify 38 duplicate images (with zero loss if removed) and 92 similar images (with  $<8.5\%$  loss if removed).

We further evaluate the loss in cell counting accuracy by enlarging the blood sample image. As shown in Figure 4, optimizing the cell image library by eliminating duplicated or similar cell images only incurs a small loss in counting accuracy regardless of the size of the blood sample image or the average count of cells. That is, the difference of cell counting results between original and optimized algorithms is sufficiently small (e.g., less than 200) even when the blood sample image is large enough (e.g., with 8000 cells).

The aggregated loss incurred by eliminating these images can be easily countered by reducing the threshold. Since the threshold value is closely coupled with the number of counted cells, it is important to reduce the threshold value, such that we can obtain the most compact library. We note that the threshold value of at least 0.6 indicates a strong correlation considering the correlation coefficient [36] [37]. Therefore, eliminating most redundant cell images from the library and adjusting the threshold value from 0.67 (current value) to 0.60 allow us to obtain the optimized library with cell images that are essential to achieve a desired accuracy.

Figure 4b illustrates the sensitivity of cell counts to a threshold value; a cluster (of a size up to  $3 \times 3$ ) indicates a cell. In Figure 4b, 24 cells are marked under a high threshold value, while 42 cells are identified after decreasing the threshold. Based on this result, we conduct an experiment with six blood sample images to develop a model to compensate for the change in cell counts. We vary the threshold value from 0.67 to 0.60, where the latter indicates the lowest value to indicate a strong relationship [37], and compute the

changes in the number of counted cells. As shown in Figures 4c and d, the number of counted cells linearly depends on, or is inversely proportional to, the threshold value; decreasing the threshold value increases the number of counted cells. Let  $C(T)$  denote the number of counted cells,  $\alpha$  the gradient,  $\beta$  the initial value and  $T$  the threshold value. Then, the following relationship holds:

$$C(T) \approx \alpha \cdot T + \beta \quad (2)$$

Equation (2) can be used to adjust the threshold value to counter the loss in counting accuracy after optimizing the library.

After the cell image library is optimized, the number of cell images in the original library is reduced from 150 to 20 with 8.5% accuracy loss on average. However, after we adjust the threshold value to 0.64 by using Equation (2) to compensate for the negative effect of fewer cell images in the library, we observe only negligible accuracy loss. Note that eliminating more cell images from the library yields noticeable accuracy loss that cannot be compensated for by simply adjusting the threshold value. With this optimized library containing only 13% ( $= 20/150$ ) of cell images compared to the original library, we reduce the runtime by 87%.

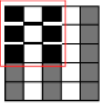
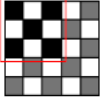
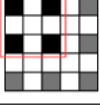
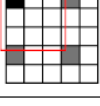
### 2.3.2 NCC Approximation

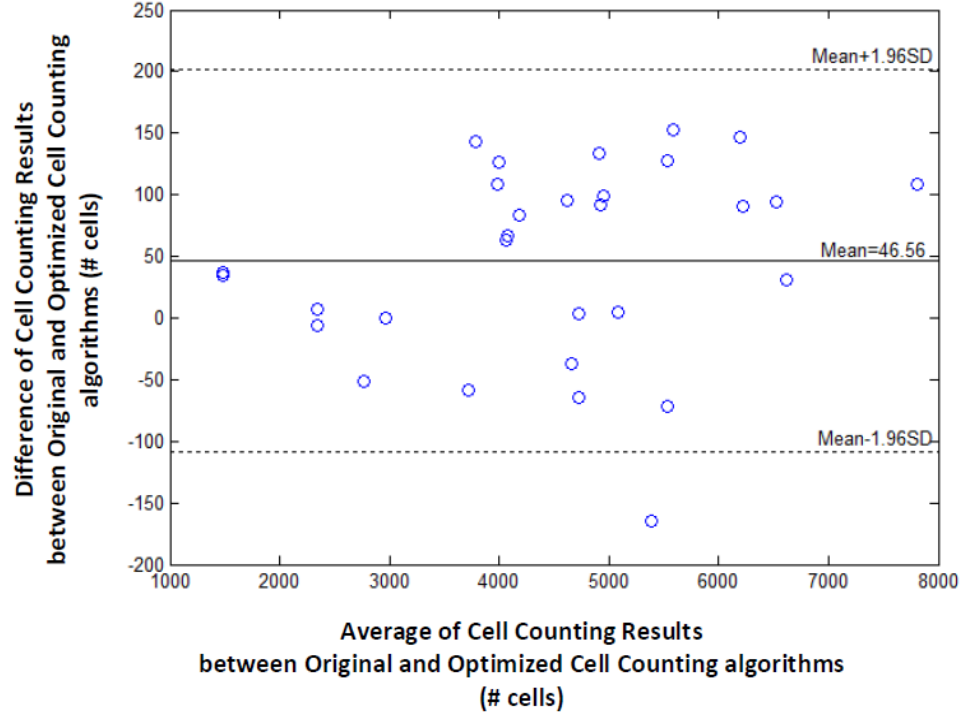
The runtime reduction of NCC approximation can be computed as follows. If NCC values are evaluated for every other point both horizontally and vertically, the runtime will be reduced to 25% of the original runtime. However, this method may slightly decrease the counting accuracy, because it does not check all of the points, taking the risk of missing points associated with the center of cells that can give higher NCC values than other points. To minimize accuracy loss for such a case, we present four heuristic patterns with the

highest detection probability for a cell, as well as the shortest runtime, as shown in Table

1.

**Table 1.** Four heuristic patterns for NCC approximation, judiciously chosen to maximize the detection probability for a cell, as well as to reduce the runtime as much as possible. Employing Patterns 1, 2 and 3 reduces the runtime for evaluating NCC values by 50% ~ 75% at the expense of some accuracy loss (1.4% ~ 6.1%). Patterns 1 and 2 yield the highest detection probability (97.1% ~ 98.6%) and maintain the same amount of runtime reduction (50%). Pattern 3 achieves further reduction in runtime (75%) compared to Patterns 1 and 2, but its detection probability becomes lower (93.9%). Pattern 4 has the poorest detection probability (50.1%) and, hence, may not meet the accuracy requirement.

Description	Pattern	Runtime Reduction	Skipped Points	Total Points	Detection Probability
Heuristic Pattern 1		50%	3	9	98.4%
Heuristic Pattern 2		50%	4	9	96.8%
Heuristic Pattern 3		75%	5	9	93.7%
Heuristic Pattern 4		89%	8	9	50.0%



**Figure 5.** The Bland-Altman plot, evaluating the accuracy of the optimized cell counting algorithm in comparison with an original algorithm. The x-axis is the average of counting results of original and optimized algorithms, while the y-axis is the difference between them. It has a bias of 46.56 cells, and upper and lower limits of 201.72 and  $-108.60$ , respectively.

As a metric to quantify the accuracy loss, a cell detection probability is derived as follows.

Let  $t (= m \times n)$  denote the total number of points in the cluster, e.g., set to nine for the maximum cluster size of  $3 \times 3$ , and  $s$  the number of skipped points in the cluster. Then, the detection probability,  $P_{K|org}$ , which is the probability that the algorithm with heuristic pattern  $k$  detects a cell within the cluster when the original algorithm has detected the cell, can be calculated by:

$$P_{K|org} = 1 - \frac{2^s}{2^t} \quad (3)$$

Table 1 presents both  $P_{K|org}$  calculated using Equation 3 and the rate of runtime reduction. The results show that employing Patterns 1, 2 and 3 reduces the runtime for

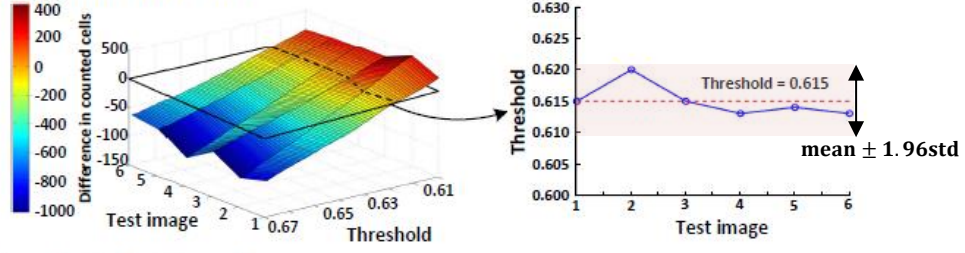
evaluating NCC values by 50% ~ 75% at the expense of some accuracy loss ( $1 - P_{K|org}$ , 1.6% ~ 6.3%). Specifically, Patterns 1 and 2 yield the highest detection probability (96.8% ~ 98.4%) and maintain the same amount of runtime reduction (50%), while Pattern 3 achieves a further reduction in runtime (75%) compared to Patterns 1 and 2, but its detection probability becomes lower (93.7%). Pattern 4 has the poorest detection probability (50.0%) and, hence, may not meet the accuracy requirement.

To compensate for the accuracy loss due to NCC approximation, we also adjust the threshold value using Equation (2), as we do for optimizing the cell image library. First, we compare the accuracy of the original algorithm with that of the algorithm with NCC approximation, both of which use the optimized cell library. Figure 5 plots the difference in counted cells between the two approaches; the closer the value is to zero, the more accurate the algorithm with NCC approximation gets. Since all four heuristic patterns for NCC approximation cross zero, it is possible to find the best threshold values that can practically eliminate the accuracy loss.

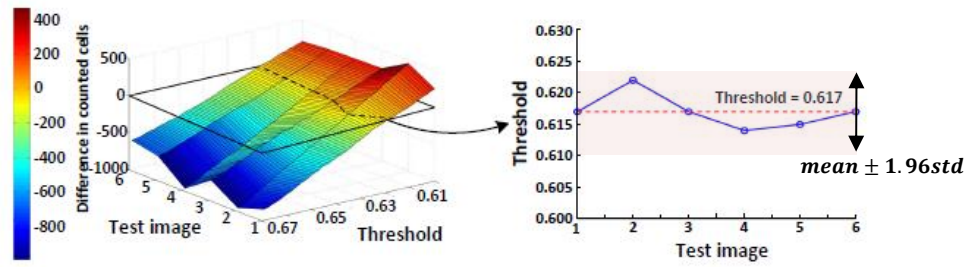
Figure 6 also presents the threshold values using four heuristic patterns for the same counting accuracy as the original algorithm. Clearly, the more points the algorithm skips, the shorter the runtime it achieves, as illustrated in Table 1. However, we need to decrease the threshold value to compensate for the increased counting loss. Our analysis shows that the heuristic Patterns 1 and 2 satisfy the accuracy requirement for the range of threshold ( $>0.6$ ). With these heuristic patterns, we reduce the runtime required for NCC by 50%.



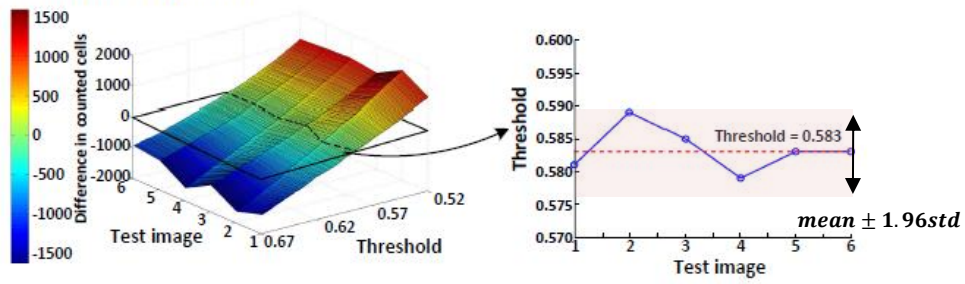
### Heuristic Pattern 1



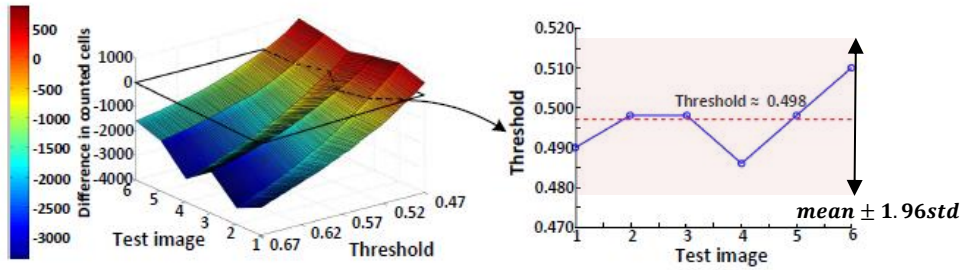
### Heuristic Pattern 2



### Heuristic Pattern 3



### Heuristic Pattern 4



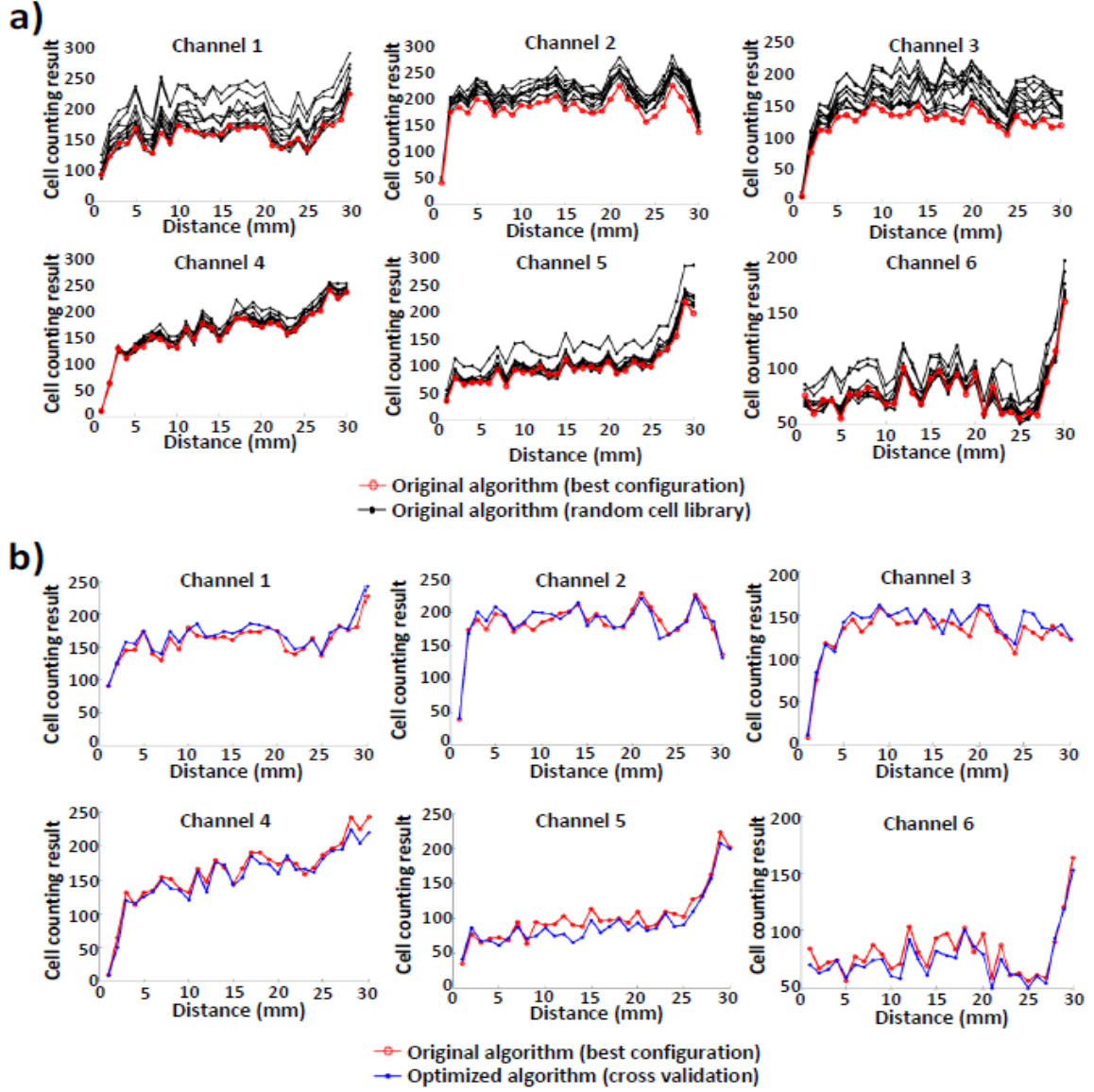
**Figure 6.** The difference in counted cells between the original algorithm and the algorithm with NCC approximation (heuristic Patterns 1~4). The closer the difference is to zero, the more accurate the algorithm with NCC approximation gets. Since all four heuristic patterns for NCC approximation cross zero, it is possible to find the best threshold values that can practically eliminate the accuracy loss, which are 0.615, 0.617, 0.583 and 0.498 for heuristic Patterns 1, 2, 3 and 4, respectively. The heuristic patterns 1 and 2 satisfy the accuracy requirement (i.e., zero loss) for the range of threshold ( $>0.6$ ) and reduces the runtime required for NCC by 50%.

### 2.3.3 Measurement Using an Android Device

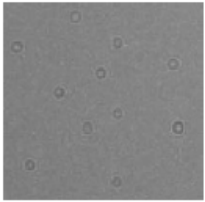
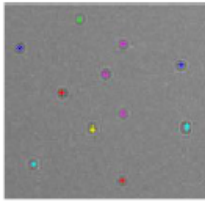
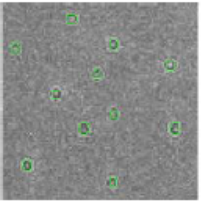

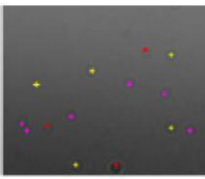

We run both the original and optimized cell counting algorithms on an Android smart phone connected to the imaging apparatus shown in Figure 3 to evaluate the effectiveness of our proposed optimization techniques for  $3334 \times 445$  blood sample images.

To compare the accuracy and runtime of the original algorithm with those of the optimized algorithm, we run the two algorithms 10 times for six channels of the blood sample image. Figure 7 shows the counting accuracy or the number of counted cells of the original and optimized algorithms. In Figure 7a, for each of six channels, 10 count results of the original algorithm, each with its own randomly-selected cell image library, are plotted based on the distance (up to 30 mm) from the inlet port of each channel; the count result of the original algorithm that yields the best match with manual counting [18] is plotted, as well. Likewise, the counting results of the original algorithm (best configuration) and the optimized algorithm (via cross-validation) are compared in Figure 7b. In the original algorithm (using 150 random cell images), the number of counted cells varies a lot (up to 30%), due to the random generation of the cell image library for each execution. By contrast, the number of counted cells in the optimized algorithm is very close to that of manual counting. The optimized algorithm exhibits an average difference of 5.05%. This demonstrates the robustness and effectiveness of the proposed approach.

Figure 8 compares NCC-based algorithms (both original and optimized) with manual counting and another cell counting algorithm [34] under two different scenarios. When



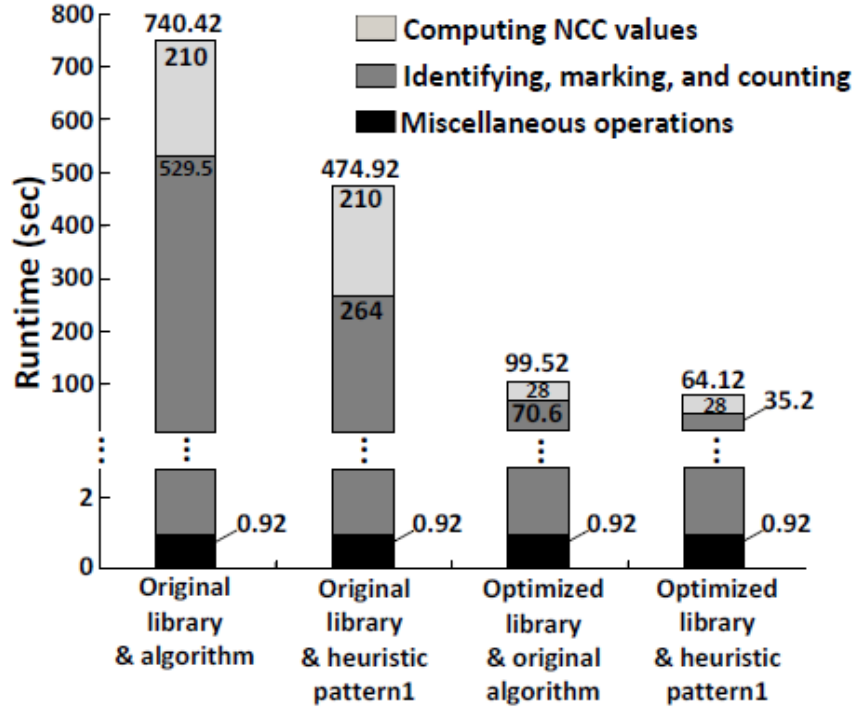
**Figure 7.** Evaluation of the counting accuracy of the original and optimized algorithms. (a) For each of six channels, 10 count results of the original algorithm, each with its own randomly-selected cell image library, are plotted based on the distance (up to 30 mm) from the inlet port of each channel; the count result of the original algorithm that yields the best match with manual counting is plotted, as well. In the original algorithm (using 150 random cell images), the number of counted cells varies a lot (up to 30%), due to the random generation of cell image library for each execution. (b) The counting results of the original algorithm (best configuration) and the optimized algorithm (via cross-validation) are compared. For each of the channels, a specific cell image library for the optimized algorithm is generated by using the rest of five channel images to conduct cross-validation. The optimized algorithm exhibits an average difference of 5.05%. This demonstrates the robustness and effectiveness of the proposed approach.

	(a) Manual counting		(b) NCC-based Automated Counting (Original & Optimized)		(c) Rapid Automated Cell counting[18]	
	Image	Count of Cells	Image	Count of Cells	Image	Count of Cells
Normal Image		11 Cells		11 Cells		11 Cells
Noisy Image with Variations in Background Intensity		14 Cells		13 Cells		N/A

**Figure 8.** Comparison with manual counting and another cell counting algorithm [34]. With normal blood sample images, all three methods have the same results. For noisy images with intensity variations, NCC-based algorithms (both original and optimized) produce counting results close to those of manual counting, while [34] fails to reliably count cells.

normal blood sample images are applied, all three methods have the same counting results. By contrast, when the blood sample image is noisy and has variations in background variations, NCC-based algorithms produce counting results that are close to those of manual counting, while [34] fails to reliably count cells. This clearly shows that the proposed algorithm reliably deals with image anomalies, e.g., variations in background intensity, brightness and noise.

Figure 9 shows the runtime of the original algorithm and three optimized algorithms employing either or both optimized cell libraries to minimize the number of cell images and heuristic Pattern 1 to skip NCC evaluations for some points, where the latter includes: (i) the optimized algorithm using NCC approximation with heuristic Pattern 1 only; (ii) the



**Figure 9.** The runtime of the original algorithm and the optimized algorithms employing either or both of an optimized cell library to minimize the number of cell images and heuristic Pattern 1 to skip NCC computations for some points. The runtime of the original algorithm that evaluates NCC values for each and every point is, on average, 740.42 s, while that of the optimized algorithm is only 64.12 s, achieving almost a  $11.5\times$  runtime reduction with accuracy loss less than 1%. The result also demonstrates that the cell library optimization reduces the runtime by 86.6% (from 740.42 s to 99.52 s), while heuristic Pattern 1 contributes to a 50.1% runtime reduction (from 529.5 s to 264 s).

optimized algorithm using cell library optimization only; and (iii) the optimized algorithm employing two synergistic techniques together. The runtime of the original algorithm that evaluates NCC values for each and every point is, on average, 740.42 s, while that of the optimized algorithm is only 64.12 s, achieving almost an  $11.5\times$  runtime reduction with accuracy loss less than 1%. The result also demonstrates that the cell library optimization reduces the runtime by 86.6% (from 740.42 s to 99.52 s), while heuristic Pattern 1 contributes to a 50.1% runtime reduction (from 529.5 s to 264 s).

## 2.4 Summary

Motivated by the need for fast and energy-efficient cell counting for mobile POC testing platforms, we proposed two synergistic techniques that optimize the cell image library and approximate the NCC-based cell counting algorithm and demonstrated their efficacy using an Android smart phone. First, optimizing the cell image library systematically eliminated duplicate and similar cell images that were manually chosen during the library creation process, reducing the runtime by nearly 87%. Second, approximating NCC evaluations by systematically skipping some points in a blood sample image also decreased the runtime by 50%. Note that a naive application of these two optimization techniques incurred some loss of counting accuracy. Thus, we developed a model for quantifying the loss of accuracy associated with these optimization techniques, and we demonstrated that such accuracy loss could be compensated for by adjusting the threshold value within an acceptable range (i.e.,  $>0.6$ ). An Android smart phone running the original algorithm with the original cell image library containing 150 cells took 740.42 s to count all of the cells in a  $3334 \times 445$  blood sample images. In contrast, the same Android smart phone running the optimized algorithm took 64.12 s with accuracy loss less than 1%, reducing the runtime by  $11.5\times$ .

### **III. Human-level Blood Cell Counting System using NCC-DEEP**

#### **LENRNING ALGORITHM on Lens-free Shadow Image**

##### **3.1 Introduction**

In biological analysis, identifying cells from a blood image is a very time-consuming task and may incur erroneous results if manually conducted [23]. Especially, in a diagnostic field based on the images and identification results, there are lots of requirements for decision making from the specialist. Until now, the wide-spread pattern recognition method is black and white classification approach such as image-J. [38]. That converts an image (i.e. 16-bit) to gray-scale, and adjusts threshold to highlight the cells as the black and white scale. Moreover, the other approaches or programs are hard to design or set parameters to properly identify cells. For a point of care testing, the platform should be integrated with functions for the help of decision making of an image specialist and doctors [23].

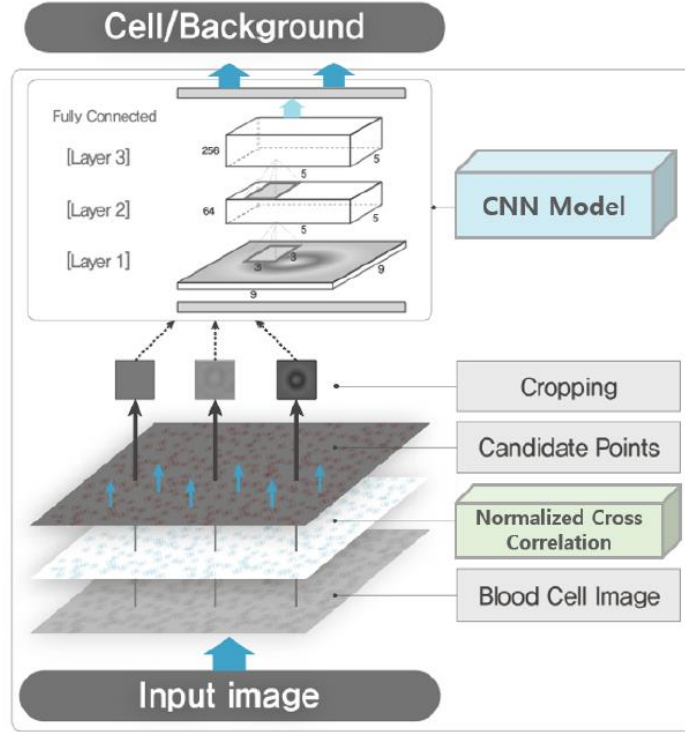
The in-line holographic imaging method is emerging imaging technology for a cell identification in the biological field [39] [40] [41]. That is a simplest holographic method working without any electric and magnetic lenses. The images can be generated from interference between reference light and shadow of the biological sample, i.e. cultured cell, white blood cell, red blood cell, or bacteria [39]. For a point of care testing without using a complex lens system, the in-line holographic apparatus for some low-cost diagnostics is a promising platform technology for a hand-held type microscope which is composed of a simple led light source and a single CMOS camera [42]. However, due to imperfectness of the optical setup, the images taken from the in-line holographic apparatus shows an irregular background intensity [43] [44] [45] and out-of-focus pattern of the targets such

as blurry cell that are hard to distinguish the cell from the background. To tackle that, the various approaches are developed to enhance the identification of the target cell from noisy images. Ra *et al.* [18] presented a cell counting approach by using normalized 2D cross-correlation(NCC) approach that achieved a robustness for irregular background. However, the NCC approach does not guarantee the robustness to the blurry cell since the pattern of the cell closes the background noise. So that, the NCC shows low precision that measure true positive ratio in predicted condition positive while high recall that is true positive ratio of condition positive. Tikkanen *et al.* [46] presented a machine learning method that is Histogram of Oriented Gradients (HOG) features with Support Vector Machine (SMV) classifier. HOG extracts clearly the shape context from abrupt edges between objects but that shows a low accuracy for blurry cell because the blurry cell provides less information available to distinguish a cell from the background [47] [48]. Liimatainen *et al.* [49] designed another machine learning method (i.e., logistic regression). While these machine learning approaches verified their excellence for the bright background, they have some disadvantage for the blurred cell since logistic regression has difficulty to distinguish blurry cells when there is the correlation between blurry cell and background noise [50].

In this chapter, we present a novel method based on normalized cross-correlation and convolutional neural network (CNN) to maximize the cell identification performance and efficiency without consuming additional hardware resources. In particular, by analyzing the correlation between normal cell, blurry cell and background noise, we defined a threshold value cause NCC process able to detect almost all cell including the blurry cell and minimal background noise as the candidate points. So that, the NCC ensures high precision and allows post process to focus solely on analyzing the results without wasting



time to enhance the images or search all point in the given blood sample image. Also, we designed CNN model to distinguish between cell or not. The CNN model is applied as the post process of the NCC and eliminates cell matching error from the candidate points. Hence, the proposed system guarantees high recall. We evaluated the proposed method for the blood sample image and that shown 0.97, 0.96 and 0.97 for the precision, recall and F1 score, respectively. That demonstrated the human-level performance ( $>0.95$ ). Also, the method enhanced cell counting efficacy up to 97.4% comparing with the CNN only algorithm.



**Figure 10.** Schematic of introduction for the NCC-CNN algorithm

### 3.2 Cell Counting Architecture

The proposed method is illustrated in Figure 10. That follows the five steps: 1) A blood sample image input to the system; 2) NCC model calculates the correlation coefficient between the sub-image on a point the blood sample and the pre-trained cell library while moving point by point. We set the size of the sub-image and the pre-trained image to  $9 \times 9$  that is able to cover almost all cell. In this process, to boost the calculation efficiency, we applied the cost effective NCC algorithm of Ahn *et al.* [51]; 3) Then, the NCC model marks the cell-like points that called candidate point where the correlation result is higher than the threshold value for identifying the candidate point. The details are in the section 3.2; 4) all the candidate points are cropped by  $9 \times 9$  sized image and that input

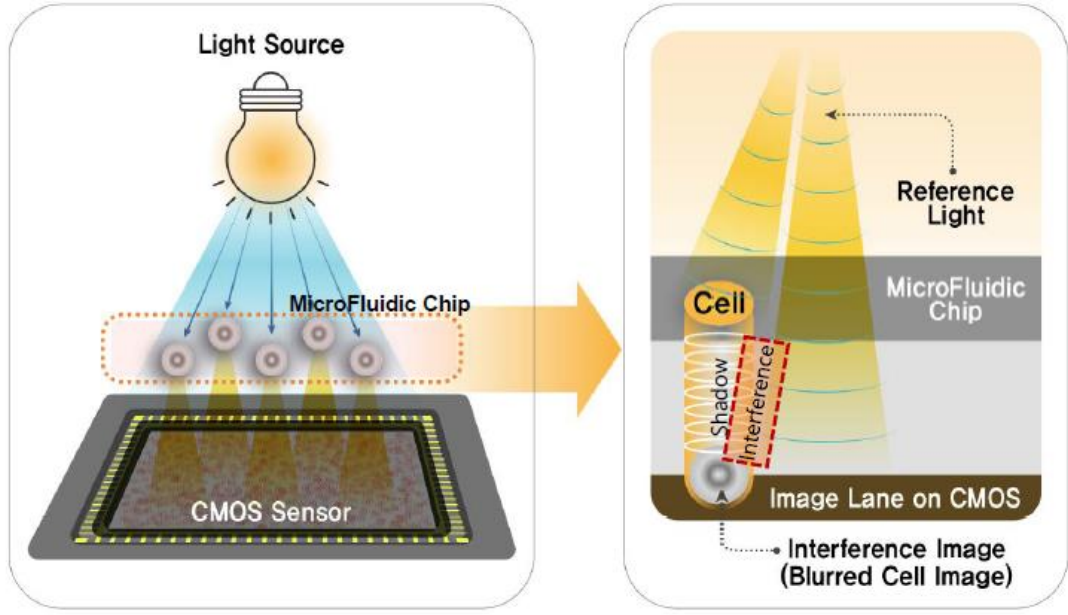
to the CNN model; and 5) the CNN model trained to identity cell distinguishes between cell or not. The details are in section 3.3. After that, the system finally counts the cell.

### 3.3 Methods

#### 3.3.1 Candidate Point Selection based on NCC

NCC is widely used in the object recognition in given a scene (i.e. face tracking while driving and license plate recognition of building management system). In this chapter, we applied the NCC to detect cells. NCC calculates the correlation between blood sample image and cell images from the pre-configured cell image library, and returns a correlation coefficient. To identify a cell, it first loads the pre-configured cell images with  $9 \times 9$  size, and calculate the correlation coefficient for the all point on the blood sample image by using Equation 4:

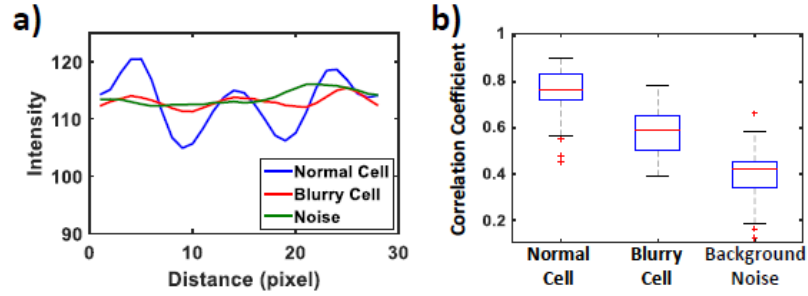
$$R(i,j) = \frac{\sum_{y=0}^{L-1} \sum_{x=0}^{K-1} (\omega(x,y) - \bar{\omega})(f(x+i,y+j) - \bar{f}(i,j))}{\sqrt{\sum_{y=0}^{L-1} \sum_{x=0}^{K-1} (\omega(x,y) - \bar{\omega})^2} \sqrt{\sum_{y=0}^{L-1} \sum_{x=0}^{K-1} (f(x+i,y+j) - \bar{f}(i,j))^2}} \quad (4)$$



**Figure 11.** Schematic print of the in-line holographic apparatus and the cause of the blurry cell image

where  $0 \leq i \leq (M - K)$  and  $0 \leq j \leq (M - L)$ .  $M$  and  $N$  is size of a blood sample image ( $M \times N$  pixel), and  $K$  and  $L$  is size of a cell image ( $K \times L$  pixel).  $w(x,y)$  and  $f(x,y)$  denote a pixel point value of a cell library and  $K \times L$  sub-image on the blood sample image, respectively. and  $\bar{w}$  and  $\bar{f}$  is a mean of each images. As a result of that, the NCC value  $P(i,j)$  has -1.0 or +1.0 when the two images have strong similarity. On the contrary, the value closes to 0 when they have highly irrelevant.

After the NCC process, the correlation coefficient values are compared to the detection threshold to identify a cell, and marks the point as a detected cell when the value is larger than the threshold. However, NCC has limitations for the blurry cell unfocused by the interference of light source, as shown in Figure 11 since NCC is not able to detect the variant features with respect to scale, rotation, focus and perspective distortions [52]. The



**Figure 12.** Intensity and correlation coefficient of normal, blurry cell and background noise

Figure 12 (a) shows the intensity of the normal, blurred cell and background noise. In the normal cell case (blue line), the intensity has 'w' shape, but the blurred cell (red line) has a slightly 'w' shape but closes background noise (green line). Based on the fact, to quantify the similarity, we evaluated the correlation coefficient in normal cells versus normal cells, blurred cells and background, as shown in Figure 12 (b). The details of the box plot are that the blue box is interquartile range (IQR) which means the spread of the middle 50% (25~75 percentile) of data values, a red line in IQR is median, the upper and lower fence of IQR is the max and min value, and '+' is outlier which is larger or less value than the upper and lower fence. In the normal cell case, the correlation coefficient has 0.76 median and 0.72 to 0.83 range of IQR. That value represents a probabilistically strong correlation [53] [54]. Also, if the detection threshold sets over 0.6, the NCC shows low false alarm since there is slight overlap between normal cell and noise. On the other hand, to detect the blurred cells, NCC is necessary to lower the detection threshold value since the blurred cell has 0.58 median and 0.38 minimum range. However, the low threshold causes false alarm since there is strong overlap between blurred cell and noise. Nevertheless, we applied the low detection threshold to detect all cells including blurry cells. Also, we considered the appropriate threshold value because the very low threshold includes many noise as cells

and that increases the computational cost for the post-processing to remove the noise. Therefore, to minimize blending of background noise while including all cells, we set the threshold to minimum value of the statistically normal distribution of the blurry cells by using the formula:

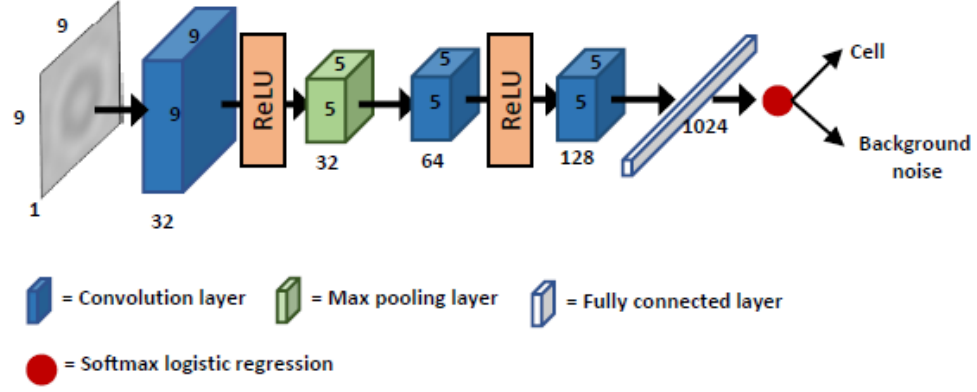
$$\text{Threshold} = Q1 - 1.5 \times \text{IQR} \quad (5)$$

where Q1 is first quartile (lower side of blue box). As a result of that, the threshold follows 0.39. Based on the fact, we can see the NCC process with the threshold calculated by Equation 5 can detect the points of almost all normal, blurry cells and some noise as cells on the blood sample image. We define the points detected by NCC as the candidate points.

### 3.3.2 Reliable Cell Counting using CNN

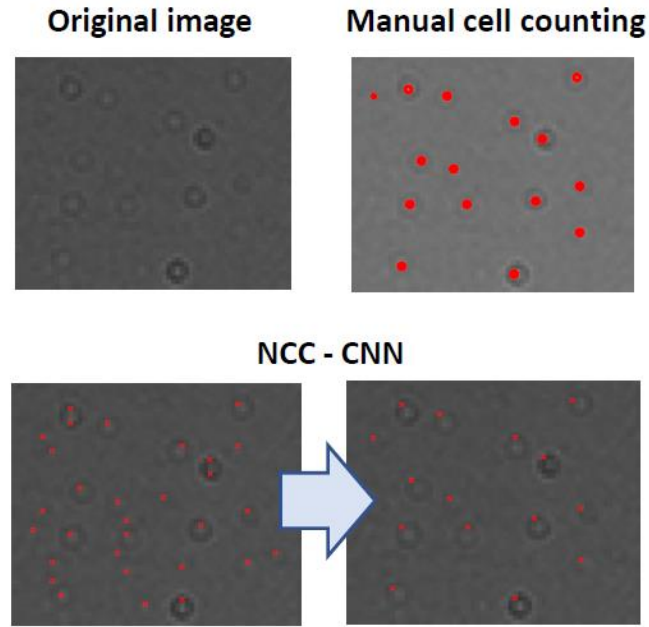
There are two conditions in the candidate points marked by NCC process. One is true positive condition if the candidate point is a cell, another is false positive condition if the candidate point is background noise. It thus is required to the post-process to identify and remove the second condition for reliable system. To achieve that, we designed CNN which is a classification algorithm based on machine learning. There are already many CNN models such as AlexNet [55], VGGNet [56], ReNet [57], but they requires expensive computational cost since the models use large size input image and filters. So that, in this study, we considered a smaller network design motivated from AlexNet.

The entire network architecture is shown in Figure 13. The network consists of three convolution layers followed by rectified liner units (ReLU) [58] and max-pooling, and a fully connected layer and a softmax logistic regression layer [59] in the last two layers. The



**Figure 13.** CNN architecture. That consists of three hidden layers with two ReLU function, a max pooling layer, fully connected layer and softmax logistic regression.

convolution layer accepts  $i \times j \times k$  image as input where  $i$  is height,  $j$  is width of cell image and  $k$  is channels, and the  $k$  is 1 in this chapter since the in-line holographic apparatus provides gray scale image. Then, the convolution layer with  $k$  filters of size  $n \times n \times m$  calculates the convolution [55] for all position on the input and produce  $k$  feature maps, where  $n$  is block size for convolution works and  $m$  equals  $k$ , and the values of a filter with  $n \times n \times m$  block are generated randomly. The ReLU is an activate function. for the convolution output on a point of input, that decides activation depending on  $f(x)=\max(0,x)$  that activates the output when only  $x$  value is larger than 0, otherwise the output is 0. Max-pooling layer performs a down-sampling operation given the output of the convolution. That has the  $w \times h$  sized spatial block and moves along the stride, discarding all values except for the maximum value in the block. The fully connected layer connects every neuron in one layer with  $1 \times (\text{previous layer size})$  size array such as the traditional multi-layer perceptron layer [55]. Finally, given the fully connected layer, the soft-max layer generates K-dimensional categorical distribution in range 0 to 1, where K is number of category.



**Figure 14.** Demonstration of NCC-CNN process

These subsequent hidden layers follow as shown in Figure 13: 1) The first hidden layer applies 32 filters of  $3 \times 3$  size followed by ReLU, and  $2 \times 2$  sized max pooling is implemented with 2 strides and outputs  $5 \times 5 \times 32$  size of data; 2) The second hidden layer uses  $5 \times 5 \times 64$  filters and follows ReLU again; 3) The  $5 \times 5 \times 64$  blob is applied by  $5 \times 5 \times 128$  followed by ReLU, and the result is connected to the fully connected layer; 4) A fully connected layer contains 1024 neurons with a ReLU; and 5) The last layer maps to cell or background noise.

Figure 14 shows a demonstration of the normalized cross correlation and convolutional neural network (NCC-CNN) process comparing with the original image including the blurry cells and manual cell counting result. Compared to the manual counting result that marked 16 cells for the test image, NCC process with the proposed threshold value selected the 31 candidate points including the all cell and 15 false positive



**Table 2.** The list of subjects to compare with the proposed algorithm. That consists of 9 algorithms based the three base types

Base type	Applying algorithm	Label
Single	Support Vector Machine	SVM
	Logistic Regression	LogR <sup>15</sup>
	Normalized Cross Correlation	NCC <sup>11</sup>
	Convolutional Neural Network	CNN
HOG base	Support Vector Machine	hogSVM <sup>12</sup>
	Logistic Regression	hogLogR
	Convolutional Neural Network	hogCNN
NCC base	Support Vector Machine	nccSVM
	Logistic Regression	nccLogR
	Convolutional Neural Network	nccCNN

points. But, based on the candidate points, CNN process identifies accurately all the cells and that shows human level cell counting result.

Through the overall system process, NCC and CNN process show the synergic operation. The proposed NCC process has the high false positive but has low false negative. That process reduces effectively the false negative rate of the CNN process. And, CNN process identifies accurately the cells among the candidate points. Also, the strategy of selecting the candidate points using the NCC process reduce drastically the cost of the CNN process because the NCC process is faster than the CNN process.

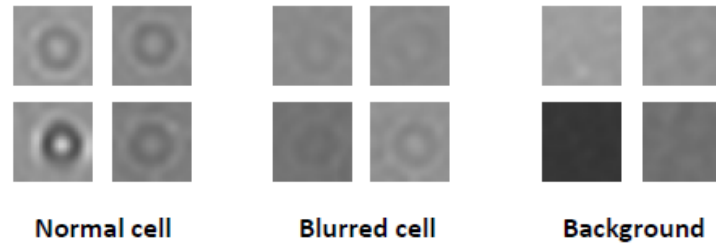
### 3.4 Results

#### 3.4.1 Subjects

For evaluating the proposed algorithm as well as comparing to other related algorithm, we build up some algorithms in Table 2. The algorithms consist of 9 algorithms based on

the types of algorithm are single, HOG base and NCC base. Some algorithms (i.e. hogSVM, LogR, NCC) are presented in [46] [49] [18]. Based on that, we added the CNN and mixed them to find the best algorithm compared with the proposed (NCC-CNN). In the evaluation environment, for the applying algorithm, we followed the preprocessing process of [46] [49] [18]. In addition, for the CNN, we have no preprocess without the cropping process as the input data. In HOG case, we had extracted the HOG features and used that for the training and validation. Finally, in the case of NCC base, we used a sufficiently low threshold ( $=0.39$ ) to increase the cell detection probability.

### 3.4.2 Evaluation for the cropped cell image



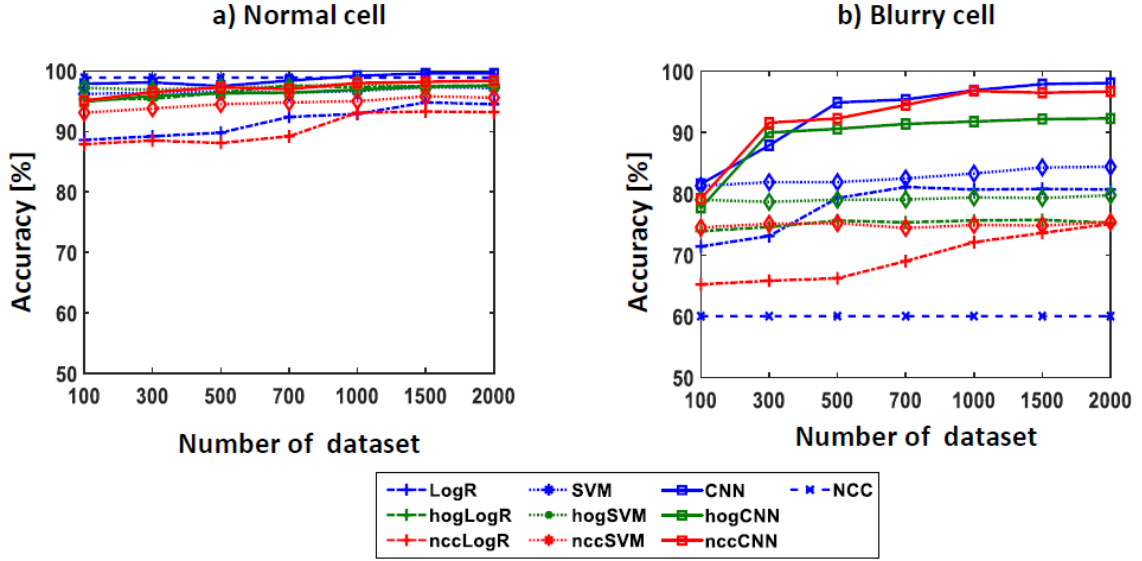
**Figure 15.** The sample images of the normal cell, blurry cell and background

we first evaluated the algorithms in Table 2 for the cropped cell image. The shape of the image is  $9 \times 9$  size image. The cropped images have the three types of label. 1) Normal cell. We defined the normal cell as an image what people see certainly as a cell; 2) Blurry cell. This is an image that looks blurry but looks like a cell, and 3) Background. It is non-cell image that seems like a noise. Figure 15 shows the sample image for each type. For

the evaluation, we collected a total of 3000 images (1000 images per each type) for the training phase, and we did the same for the validation dataset.

Figure 16 shows the performance of each algorithm while increasing the number of training datasets from 100, 300, 500, 700, 1000, 1500 to 2000. Figure 16(a) shows the evaluation result between the normal cell and the background. In this case, while LogR, SVM and nccLogR had shown the low accuracy when the learning data is small (i.e., 100~300), they have shown the increased accuracy with the increasing learning data. On the other hand, CNN and NCC show high accuracy from the initial stage. Overall, all algorithms were able to detect the normal cells with an accuracy of over 95%. Despite the noticeable performance, all algorithms without the CNN-based application drop under an accuracy of 90%.

In particular, we can see that HOG-based algorithms have lower accuracy than the other basis. The reason for that is because blurry cells have a circular shape, but, some features lose, and some features cannot be extracted. Some filters extract images similar to

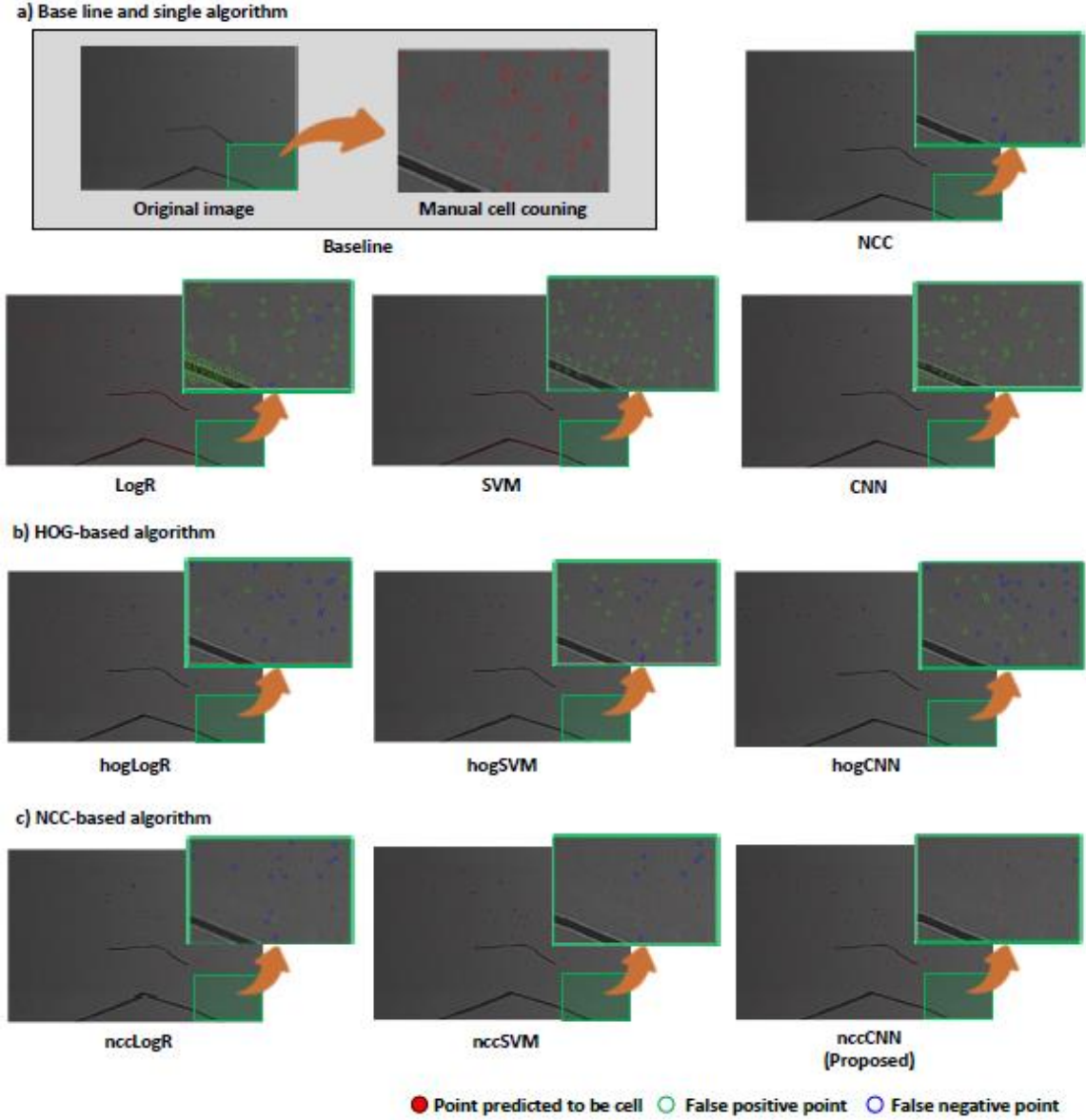


**Figure 16.** The performance of each algorithm while increasing the number of training dataset. a) is for normal cell image and b) is for blurry cell image

background images during application. Nonetheless, CNN still achieves over 95% performance by accurately learning the entire pattern of the HOG. The performance difference between the NCC and the basic algorithm is 0.86 to 3.66% of the performance drop due to the accumulation of miss errors as each algorithm checks again for images that are missed in NCC and correctly recognized as cells in NCC.

### 3.4.3 Evaluation on the blood sample image

We evaluated each algorithm for the 10 blood sample images. The test image used in the evaluation has 600×400 size, and some images have the specific points that we called 'black line'. The blood sample image may or may have the black lines depending on the experimental environment. For the evaluation, we used algorithm trained with over 1500 training images to get the best performance without any pre- and post-process such as the



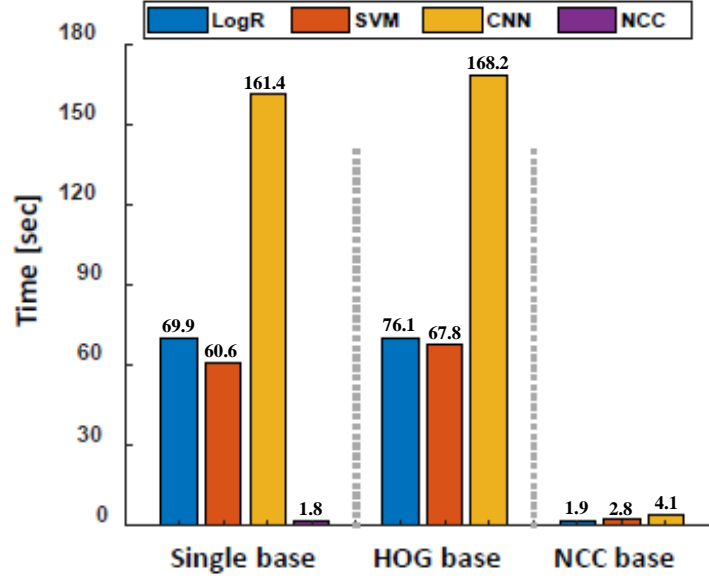
**Figure 17.** The original image, manual cell counting result and the demonstration of each algorithm

background subtraction [60] to remove the background noise since that could cause of loss of the cells. Thus, without any other preprocessing, all algorithms identify a cell from the cropped image while moving  $9 \times 9$  block to the pixel by pixel, and mark a point when the point is predicted to a cell. After every search to identify the cells, we evaluated the system by comparing the result with the manual counting result.

**Table 3.** The evaluation result of each algorithms on the blood sample image

Algorithm	Precision (.)	Recall (.)	F1 Score
LogR <sup>15</sup>	0.44	0.92	0.60
SVM	0.59	0.96	0.63
NCC <sup>11</sup>	0.98	0.81	0.89
CNN	0.75	0.97	0.85
hogLogR	0.59	0.76	0.66
hogSVM <sup>12</sup>	0.83	0.58	0.68
hogCNN	0.78	0.83	0.80
nccLogR	0.96	0.83	0.89
nccSVM	0.96	0.87	0.91
nccCNN (Proposed)	0.97	0.96	0.97

Figure 17 and Table 3 show a demonstration of each algorithm and the evaluation results, respectively. Figure 17a indicates baseline and the demonstration results of single algorithms. In this case, LogR, SVM and CNN shown ineffective for distinguishing between cell and background noise since they considered most all the convex region to cell. As a result, they had many false alarms with 0.44, 0.59 and 0.75 precision while they had high recall of 0.92, 0.96 and 0.97, respectively. Also, because of the low precision, they did not distinguish completely the black line as the background noise and marked a lot of point in that region. On the other hand, NCC had high precision (i.e. 0.98) but lower recall since that do not guarantee the robustness for specific cells (i.e. some normal cells and blurry cells). On the contrary, in hog-based case as shown in Figure 17b, hogLogR, hogSVM and hogCNN showed higher precision and lower recall comparing with the single algorithm. The reason for that is HOG extracts and provides exactly the shape features of normal cell with strong gradient in localized portion. So that, the false alarms are decreased,



**Figure 18.** The elapsed-time of each algorithm

and the algorithms provide high precision (i.e. 0.59, 0.83 and 0.78 for LogR, SVM and CNN, respectively). However, in the blurry cell case that has no clear edge context, HOG did not extract completely the feature. They thus make miss detections and have low recall (i.e. 0.76, 0.58 and 0.83 for LogR, SVM and CNN, respectively). Throughout the single and hog-based algorithm, as you can see in Table 3, despite of their high precision or recall, they provide low F1 score with 0.73 averagely. Figure 17c refers to the ncc-based algorithms. NCC with low threshold contain some background noise but guarantee high recall by elect almost all cells as the candidate points. As a result of that, all the algorithms shown 22~52% higher precision and 7~13% higher recall, and nccCNN achieved 97% of F1 score that is 6~36% higher than others.

### 3.4.4 Elapsed-time evaluation

We finally evaluated the elapsed-time. The evaluation environment is Apple Macbook (MJLT2KG/A model) [61] that has intel(R) core(TM) i7-4870HQ CPU @ 2.50GHz, 16GB RAM, Windows 10 OS and no GPU acceleration. Figure 18 shows the average elapsed time of each algorithm when we ran out the algorithms on a blood sample images. Based on that, we can see the single algorithms without NCC spend time more than 60s to get the cell counting result, LogR, SVM and CNN show the elapsed time of 69.96, 60.69 and 161.4s, respectively, and NCC spends 1.86s. Also, In the case of HOG base, they require more time than single base since the HOG process is added to a single algorithm's process. As the result of that, LogR, SVM and CNN show 76.1, 67.85 and 168.2s, respectively, which increased by 0.1 to 10.5% from the single base. On the other hand, NCC saves dramatically the elapsed-time. With NCC process, LogR, SVM and CNN have 1.95, 2.81, 4.12s, respectively, which decreased by 96.7% on average.

### 3.5 Summary

Most previous methods to address the cell counting problem has focused on counting cell under a constraint which is the varying of the background images (i.e. bright field). However, the lens-free in-line holographic apparatus provides the problem as well as out-focus problem which produces blurry cells. In this chapter, we designed NCC-CNN to achieve effectively the problems. The proposed algorithm searches and marks the candidate point on the cell-like point by using NCC set to a low-threshold, and CNN model trained by distinguishing between cell or not identifies and count cells from the candidate points. The proposed algorithm trained with more than 1,500 training data showed 96.6%



accuracy when evaluated in cropped images (i.e. normal cell, blurry cell and background image), and exposed the 12.1~36.6% improved performance from the NCC, LogR and SVM, and a difference of 1.3% from CNN alone. In the evaluation for the blood sample image, the NCC-CNN exhibited 97% performance, which was 6~37% improved performance compared with others. Finally, we evaluated the elapsed time, and the NCC-CNN showed 4.12s which is 40 times faster than the CNN-only algorithm.

The suggested cell identification method is using a machine learning approach to eliminate cell matching error and to provide cost-effective calculation of the biological images. This approach also does not require a complex and time-consuming parameter setting to recognize or identification of the biological target. This merit can serve that a biologist tries not to an enhancement of image or identification but to focus on analysis result with high accuracy.

## **IV. Smart Gait-Aid Glasses for Parkinson's Disease Patients**

### **4.1 Introduction**

Parkinson's disease (PD) is a chronic progressive disease that degenerates the nervous system of a patient losing dopaminergic neurons in substantia nigra of the brain [62]. PD is most common for adults over 60 [63]. Approximately seven to ten million people worldwide suffer from PD [64], and the number of PD patients has been increasing with the aging population. While PD symptoms vary across patients, the primary symptoms are tremor, bradykinesia, rigidity, and postural instability, all of which can disturb the gait of patients [65] [66].

Freezing of gait (FOG), which is a form of akinesia [67], is defined as brief, episodic absence or marked reduction of forward progression of the feet despite the intention to walk [68]. PD patients are likely to suffer from FOG in various daily activities, e.g., when they initiate gait, turn corners, change gait directions and/or speeds, stand up from their seats, pass along different floor patterns, and are in narrow spaces [69] [70]. Upon occurrence of an FOG episode, most PD patients feel defenceless against sudden freezing [71], making the patients experience difficulty in walking with normal gait [72] and thus negatively affecting their daily activities. In particular, FOG is a huge risk factor for falls in PD patients who get seriously hurt in the worst case [73].

Previous studies have demonstrated that rhythmic auditory or visual cues can aid the PD patients' gait [74] [75] [76] [77] [78] by breaking the freezing [79] [80], thus improve the quality of patients' daily lives. While it is not evident whether or not the auditory cues are effective for PD patients experiencing FOG [81], it was demonstrated that visual cues such as stripe lines, checkered tiles, and footprints on the floor can improve gait

characteristics such as velocity, cadence and stride length upon occurrence of FOG episodes [82] [83]. Using visual cues, a risk of developing FOG within 2 years can be predicted as well [84].

In this research, taking sensor fusion and markerless augmented reality (AR) techniques, we develop a smart gait-aid system implemented in smart glasses. Our smart gait-aid system monitors a PD user using smart glasses' inertial sensors (i.e., accelerometers and gyroscopes) and processing capability to detect FOG episodes. Upon detection of FOG episodes, it automatically triggers a visual guidance function that projects user-specific stripe patterns [70] on the floor seen through the glasses.

More specifically, we make the following key contributions. First, we develop a real-time FOG episode detection system in smart glasses for the first time. Compared with existing detection systems where sensors are located at the lower body of users, our detection system uses sensors embedded in smart glasses (i.e., mounted on the head). This poses unique challenges for accurately detecting FOG episodes with limited processing capability of smart glasses.

Second, exploiting the inertial sensors and processing capability of smart glasses, we develop a smart AR-based visual guidance system that can adaptively project visual cue patterns depending on how fast a user moves and where the user's head directs. Such adaptive projection of the patterns on the glasses is critical to maximize the effectiveness of the gait aid and minimize the interference of the user's sight with the patterns, but it also presents significant challenges because of the difficulty in precisely estimating the walking distance based solely on the head-mounted sensors as well as the limited processing capability of smart glasses.

Finally, we demonstrate the effectiveness of our system through experiments involving ten PD users to measure the accuracy of FOG detection. Our experiments show the FOG detection accuracy of as high as 92.86% and the gait speed and the stride length improvements of 15.3~37.2% and 18.7~31.7%, respectively.

## **4.2 Related Works**

Although PD symptoms can be alleviated by medications like Levodopa (L-dopa), such medications may cause tolerance and side effects [85] [86] [87]. Another method of relieving the symptoms of PD is brain surgery such as deep brain stimulation (DBS), but the surgery accompanies high risks and cannot completely cure PD patients [88] [89]. Hence, various studies have been performed to improve the patients' daily lives without medications and surgery; an overview of clinical studies regarding the intervention of FOG rehabilitation and PD gait was presented in [78]. In this section, we discuss previous studies on detecting FOG episodes and developing gait-aid systems.

### **4.2.1 Existing FOG Detection Methods**

Recently, a number of FOG monitoring systems based on inertial sensors have been developed [69] [79] [90] [91] [92] [93] [94] [95]. Moore *et al.* demonstrated that FOG episodes can be detected by analyzing the frequency spectra of readings from accelerometers attached to an ankle with a sampling rate of 100 Hz [69] [90]. In this method, a freeze index (FI) is calculated as a ratio of the power spectral density (PSD) in the *freeze* band (i.e., 3~8Hz) to the PSD in the *locomotor* (or normal movement) band (i.e., 0.5~3 Hz)

during a certain time window (e.g., 6s). Since the PSD in the *freeze* band increases during FOG episodes, it can determine that an FOG episode has occurred if consecutive FI values are above the freeze threshold. The accuracy of this method is around 78%. Based on Moore's method [69] [90], Jovanov *et al.* developed a real-time FOG detection system, in which an inertial sensor with a sampling rate of 200Hz is mounted on the right knee [79]. This system uses a time window of 320ms for real-time implementation and has the average and maximum detection latency values of 332ms and 580ms, respectively.

Niazmand *et al.* demonstrated that FOG episodes can be detected by using five accelerometers embedded into pants (i.e., the right and left thigh, shanks, and bellybutton) with a minimum sampling rate of 20Hz [91]. If the highest frequency of the dominant power from PSD of the sensor data is over 3.5Hz, the state is defined as an FOG episode. Hence, an FOG episode is detected when the number of pulses and the duration of foot shaking extracted from the sensor data are larger than their respective threshold values. This method uses a window of 2s and has sensitivity and specificity values of 88% and 85%, respectively.

Coste *et al.* proposed another criterion, called FOG criterion (FOGC), for detecting an FOG episode based on cadence and stride length calculated from accelerometric and gyroscopic data [92] since an FOG episode may occur if the cadence increases and the stride length decreases. In their method, FOGC at time  $t$  is given by  $FOGC_t = \frac{C_t \cdot L_{min}}{C_{max} \cdot [L_t + L_{min}]}$  where  $C_{max}$  and  $L_{min}$  are the maximal value of cadence and the minimal value of stride length while  $C_t$  and  $L_t$  are the measured values of cadence and stride length at time  $t$ , respectively.

#### 4.2.2 Existing Gait-Aid Systems

Nieuwboer *et al.* showed that cueing-based training has specific effects on gait, freezing, and balance [76]. Mazilu *et al.* reported that training with a cueing device upon occurrence of FOG decreases both FOG duration and frequency [95]. As such, several systems have been developed for PD patients and they provide auditory or visual cues for patients who experience FOG episodes [77] [78] [81] [96] [97] [98] [99].

Hausdorff *et al.* demonstrated that rhythmic auditory stimulation (RAS) reduces stride-to-stride variability as well as improves stride length [77]. **WalkMate** is an archetypal system that provides RAS based on the timing of footsteps for its user through headphones [96]. Hove *et al.* demonstrated that interactive RAS assisted by foot-mounted sensors offers more enhanced gait for patients than non-interactive RAS with a fixed tempo. Although Hove *et al.* showed that the gait of patients can be improved by auditory cues using **WalkMate** [99], it is not evident whether or not the auditory cues alone are effective [81]; it is speculated that effective auditory cues vary across patients.

In contrast, it was demonstrated that patients improve their gait when they walk as though they climb along visual cues such as regular floor patterns [100]. Park *et al.* showed the effect of providing visual cues on the gait of patients [70]; when patients follow the steps over a line drawn on the ground, their gait characteristics such as velocity, cadence and stride length are improved compared with the baseline without using any visual cues.

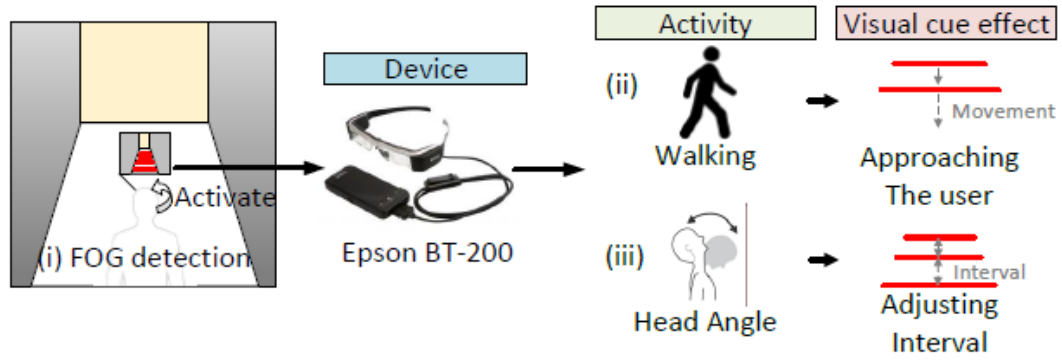
The same principle is applied to a visual laser beam stick such as **Laser Cane** [101]. **Laser Cane** projects a red line along a user's path when it touches the ground; it is lightweight and relatively energy-efficient.

There are some glasses-type devices such as *optical stimulating glasses (OSGs)*, *PD Glasses* and *GaitAid Virtual Walker*. *OSGs* provide optical stimuli in the peripheral field of view [102], where the optical stimuli is produced by continuous optical flow generated by vertical lighting lines scrolling backward or forward, or lighting stimuli synchronized with footsteps through switches attached under the feet. *PD Glasses* generate visual cues running horizontal stripe patterns on a white background which have adjustable speed and stride by hand [103]. *GaitAid Virtual Walker* is a device providing both visual and auditory cues for patients [80] [83]; it produces sound in pace with patient's stride while displaying black and white checkered tiles on the glasses.

However, all of existing devices cannot give perspectives to the projected patterns and *PD Glasses* and *GaitAid Virtual Walker* may significantly interfere the patient's sight with displayed patterns. Moreover, the gaze of the patient wearing glasses to provide visual patterns is stuck on the patterns themselves. This makes it very difficult for the patient to be aware of objects or obstacles which are hidden behind the visual patterns while walking, and thus increases the risk of injury inflicted by a collision between the patient and obstacles on the path.

### 4.3 Methods

The smart glasses device we use is Epson's Moverio BT-200, an Android platform. We choose BT-200 over popular Google glasses because BT-200 is more suitable for our purpose. That is, it is difficult for a wearer of Google glasses to look at the floor through the screen because its screen is positioned slightly above the sight and it has a monocular display. BT-200 consists of a headset, a control unit, and cables. The resolution and weight of its headset are 960×540 pixels and 88 grams, respectively. It has a built-in camera

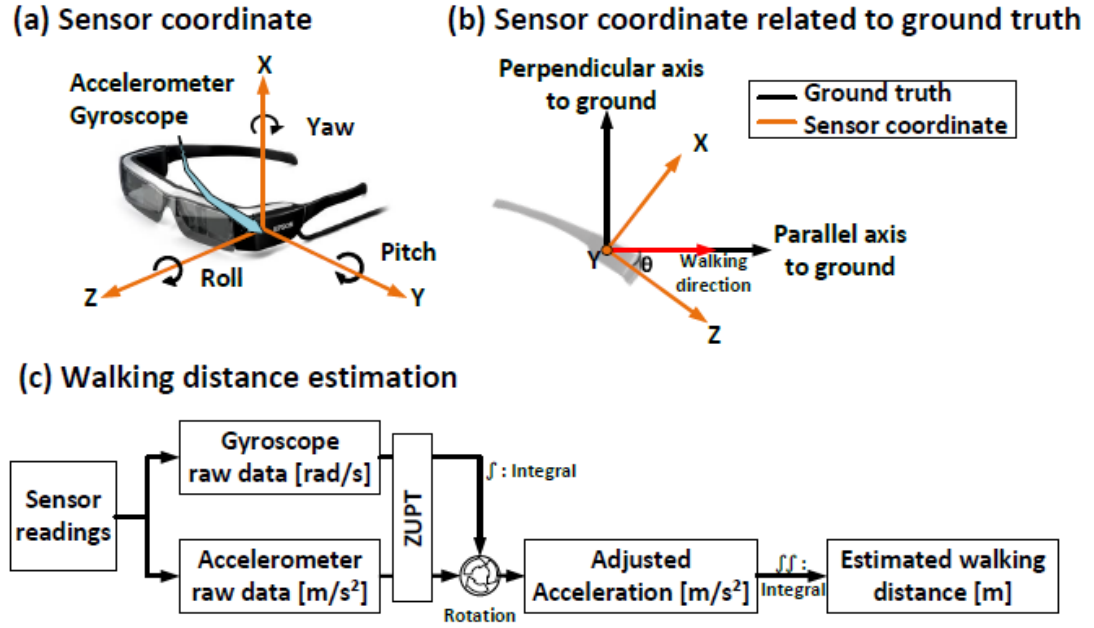


**Figure 19.** Smart gait-aid system consisting of freezing of gait (FOG) detection and movement recognition subsystems.

providing 640×480 pixels/frame and 15 frames/second. It is also equipped with inertial sensors, an accelerometer and a gyroscope with a maximum sampling interval of 0.02 [sec]. The control unit runs Android 4.0 and has a 1.2GHz dual-core TI OMAP 4480 CPU, 1 GB RAM and 8 GB flash storage.

Our smart gait-aid system based on BT-200 monitors the user's movement using the inertial sensors, and projects visual patterns as if the patterns were actually on the floor. Figure 19 gives an overview of the proposed system. The system responds to three types of activities and takes the following actions: (i) automatically project the visual cue on the screen when an FOG episode is detected; (ii) redraw the visual cue such that the visual cue looks closer to the user as the user walks; and (iii) adjust the interval of visual cues following movements of the user's head. The visual cue lasts until the wearer terminates the visual guidance. A wearer can turn on or off the visual guidance system by touching the controller pad of smart glasses. We detail each of the components in the following subsections.





**Figure 20.** (a) Sensor coordinates (3D) where the z-axis is the wearer's gaze direction; (b) sensor and global coordinates (2D) with respect to the gaze and walking direction, respectively; and (c) walking distance estimation that transforms sensor readings from into global coordinates.

#### 4.3.1 Movement Recognition

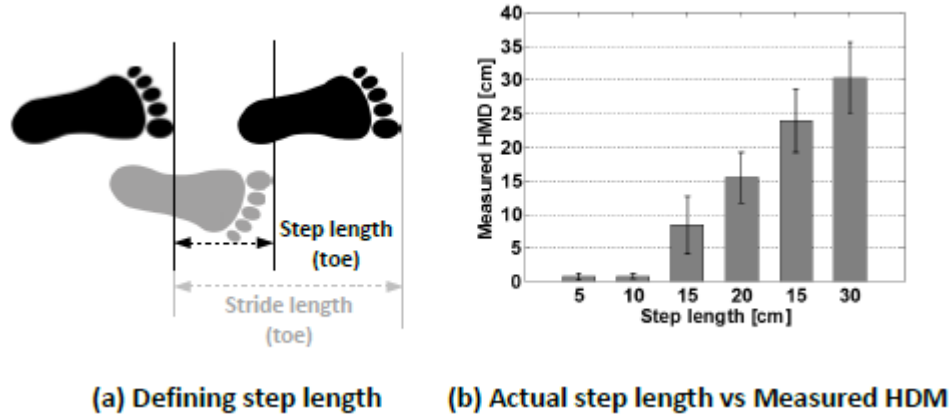
The user with PD would respond more strongly to visual cues if a visual cue appears to move closer to the user as if the patterns were embedded on the floor [104]. But the visual cue used in the previous studies [103] [80] moves independently of or inconsistently with the user's head motion. This means the user cannot fully take advantage of the visual cue. Hence, the system needs to recognize the user's walking distance and the angle of head to realistically integrate the visual cue with the scene to maintain consistency between virtual and real spaces. One may consider various image processing algorithms to meet this requirement, but it is very difficult to realize real-time video processing in smart glasses because the existing algorithms require significant computing capability. For example,

when we implement a canny edge detection algorithm in a smart phone (Samsung Galaxy S5), which has more computing capability than smart glasses, we observe the frame rate drops from 15 to 4 frames/second and buffering frames takes place.

Faced with such a challenge, we propose a lightweight system to refresh the visual patterns on the screen by estimating the user's walking distance based solely on inertial sensors of glasses. Specifically, we (i) integrate acceleration values from a built-in accelerometer of the user to precisely estimate the walking distance; (ii) compute the difference between two integrated gyroscope values in two consecutive (i.e., previous and present) frames; and (iii) use it to adjust the visual patterns on the screen.

Figure 20a shows the sensor coordinates of smart glasses and the corresponding axis values for roll, pitch and yaw, where the  $z$ -axis value represents the roll angle and the wearer's gaze direction. Figure 20b depicts the relationship between sensor and global coordinates where the former is relative to the gaze direction while the latter the walking direction. We note that the acceleration value is affected by the pitch angle of the smart glasses because the accelerometer has gravitational acceleration. That is, when the wearer looks at the ground as in Figure 20b, the  $x$ -axis component of acceleration decreases compared to the wearer looks ahead. Hence, the calculated walking distance values differ from the actual walking distance although the wearer walks the same distance. To compensate this, we rotate the acceleration vectors with respect to the pitch angle of glasses derived from a gyroscope value; from Figure 20b, we know that the  $x$ - and  $z$ -axes have to be as rotated as the pitch angle,  $\theta$ .

If the sensor coordinates are rotated relative to the ground, an accurate walking distance value from the  $z$ -axis component can be computed. To do so, we develop a walking



**Figure 21.** (a) Definition of step length; (b) step length vs. head moving distance (HMD)

distance estimation algorithm depicted in Figure 20c. The algorithm continuously reads the gyroscope and accelerometer values. We use the zero-velocity update algorithm [105] to overcome a drift problem that causes positioning errors in determining the current walking state as either stationary or non-stationary. We then recognize the stationary state between steps to segment the steps. Also, for a non-stationary state, the system uses Equation 6 to calculate the angular rotation where  $\theta_t$  and  $\theta_{t-1}$  are the current and previous angles and  $g_{y,t}$  is the current angular velocity of y-axis of gyroscope at time  $t$ .

$$\theta_t = \theta_{t-1} + g_{y,t} \quad (6)$$

Given  $\theta_t$ , the  $x$ - and  $z$ -axes of sensor coordinates are rotated by Equation 7:

$$\begin{bmatrix} a'_{x,t} \\ a'_{z,t} \end{bmatrix} = \begin{bmatrix} \cos\theta_t & -\sin\theta_t \\ \sin\theta_t & \cos\theta_t \end{bmatrix} \cdot \begin{bmatrix} a_{x,t} \\ a_{z,t} \end{bmatrix} \quad (7)$$

where  $a_{x,t}$  and  $a_{z,t}$  represent the current  $x$ - and  $z$ -axis acceleration values of the accelerometer, and  $a'_{x,t}$  and  $a'_{z,t}$  denote the adjusted acceleration. Once the acceleration values are rotated, the  $z$ -axis component is in parallel with the walking direction.

Subsequently the system can estimate the walking distance by integrating the acceleration values using Equation 8:

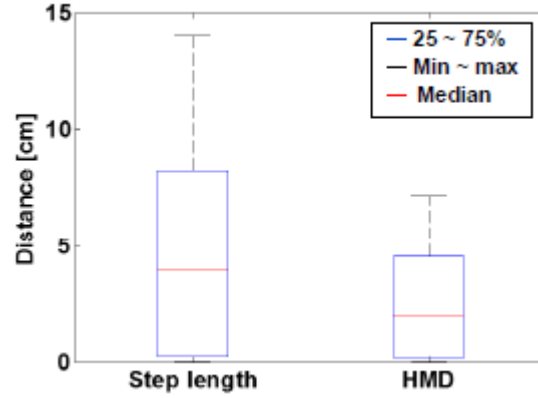
$$D_t = \iint a'_{z,t} \cdot \left(\frac{m}{t^2}\right) dt^2 \quad (8)$$

By using this walking distance estimation algorithm, the system can response to the accurate walking distance regardless of the pitch angle of head.

To validate the walking distance estimation algorithm on glasses, we conduct walking tests by changing the step length (defined in Figure 21a). The step length is set to 5, 10, 15, 20, 25, and 30cm, respectively, in each test of walking 30 steps in even strides. In order to accurately impose the specified step length, the subject steps on actual lines which are placed along the walkway at intervals equivalent to the step length. We compare the actual moving distance with the measured head moving distance (HMD) where the latter refers to the walking distance estimated in smart glasses. Figure 21b shows that the walking distance estimation algorithm has an error of  $> 20\%$  when the step length is shorter than or equals to 20cm, and an error of  $< 10\%$  when the step length is 25cm or larger. We observe that HMD gets further attenuated in the range of 5~15cm, which mostly includes steps due to FOG, because the smart glasses are not accelerated enough to estimate the real distance.

#### 4.3.2 FOG Detection On Glasses

Moore *et al.* define the freeze index (FI) to identify FOG episodes. The FI uses the ratio of the freeze band power to the locomotor band power in the frequency domain [69]. However, there are two reasons that such an approach cannot be applied directly to smart glasses. First, some PD patients have head tremor that has similar frequency (4~6Hz) to



**Figure 22.** Measured step length (obtained by using a system [48]) and HMD before FOG episodes

the freeze band, causing false-positive detections. Consequently, this approach cannot be used for such patients. Second, even if this approach is applied to PD patients with no head tremor, it requires to choose a patient-specific FI threshold value.

Coste *et al.* introduce an approach using FOGC, detecting FOG episodes based on stride length and cadence that are calculated with data acquired by foot-mounted sensors [92]. However, such an approach has limitations in dealing with unusual situations. For instance, the PD patient would have the intention to move forward when walking regardless of the occurrence of an FOG episode, which may cause a sudden long step (i.e., over 10cm). But, unfortunately, FOGC cannot detect this kind of FOG episodes.

To remedy this deficiency, we present a lightweight FOG detection system, called **FOG Detection On Glasses (FOGDOG)**, tailored for smart glasses. Like FOGC,

FOGDOG is based on the hypothesis that the cadence increases while the HMD on smart glasses decreases during an FOG episode [106]. By contrast, FOGDOG introduces the maximum value of HMD,  $\eta^{max}$  per step to minimize the degradation in FOG detection accuracy due to a sudden long step.

Figure 22 plots the statistics of measured step length and HMD during FOG episodes where the step length is obtained by using a gait tracking system of [107]. Note that the results are drawn from 30 trials. The figure shows that the mean and standard deviation values of HMD are 4.05 and 2.72cm, respectively. Based on these values, we set  $\eta^{max}$  to 10cm ( $\cong 4.05 + 1.96 \cdot 2.72$ ), which corresponds to an agreed range limit [108]. FOGDOG calculates  $D_t$  using Equation 8 and estimates HMD values, i.e.,  $D_{t,i}^{step}$  for the  $i^{th}$  step, in a sliding window of 1s at time  $t$  using consecutive peak values when the wearer places a foot on the ground. FOGDOG further adjusts HMD values due to long steps that exceed  $\eta^{max}$  using Equation 9:

$$D_{t,i}^{step*} = \begin{cases} D_{t,i}^{step}, & D_{t,i}^{step} < \eta^{max} \\ \eta^{max}, & D_{t,i}^{step} \geq \eta^{max} \end{cases} \quad (9)$$

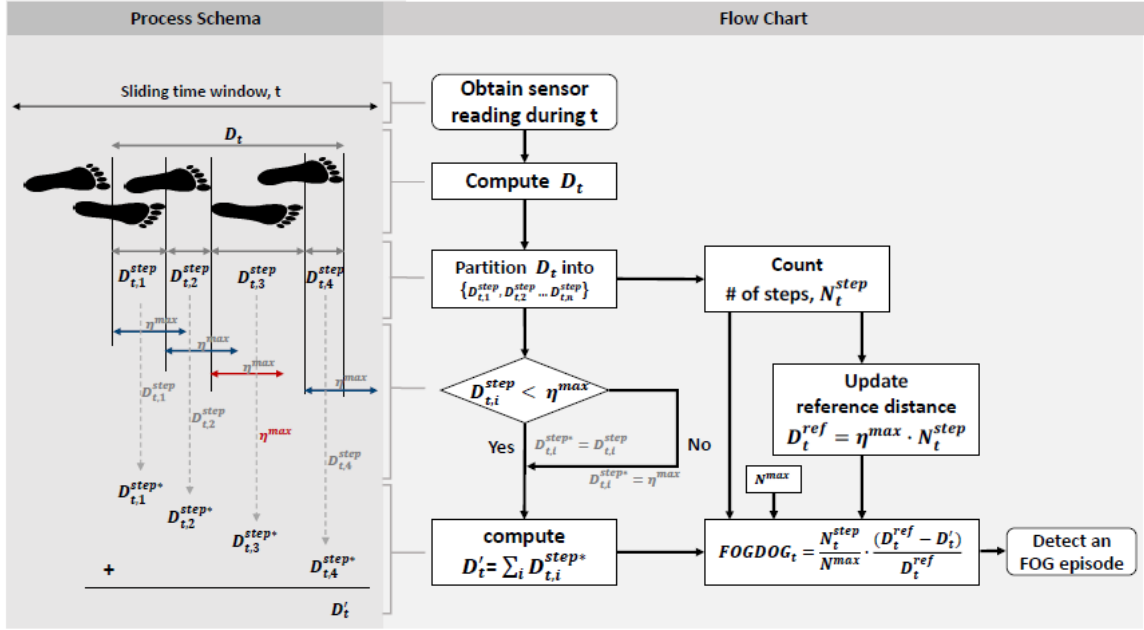
where  $\eta^{max}$  also serves as a threshold value to distinguish between normal and abnormal walking since  $D_{t,i}^{step*}$  is equal to  $\eta^{max}$  when a PD user walks normally. Based on this fact, we set a reference distance,  $D_t^{ref}$  as follows:

$$D_t^{ref} = \eta^{max} \cdot N_t^{step} \quad (10)$$

where  $N_t^{step}$  is the number of steps in the sliding window. This means  $D_t^{ref}$  is dynamically changed in proportion to the number of steps. In order to detect an FOG episode, FOGDOG compares  $D_t^{ref}$  with  $D'_t$ , where  $D'_t = \sum_i D_{t,i}^{step*}$  during the interval of  $s$ . For instance, when a person walks 4 steps,  $D_t^{ref}$  becomes 40cm. Hence, if the person walks normally,  $D'_t$  approaches  $D_t^{ref}$ , otherwise,  $D'_t$  has a smaller value than  $D_t^{ref}$ .

Next, we define a new FOG detection criterion,  $FOGDOG_t$  at time  $t$  as follows:

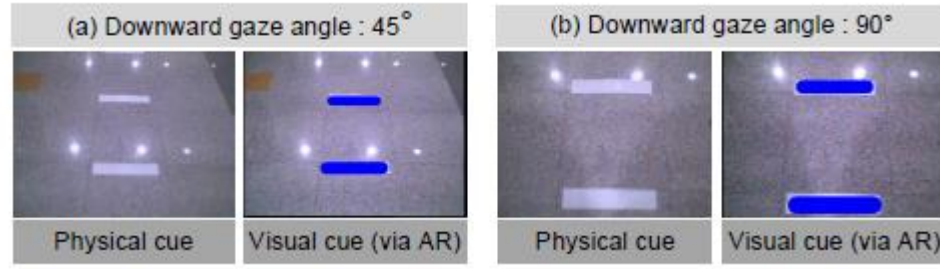
$$FOGDOG_t = \frac{N_t^{step}}{N^{max}} \cdot \frac{(D_t^{ref} - D'_t)}{D_t^{ref}} \quad (11)$$



**Figure 23.** FOG detection process of FOGDOG: it first computes the walking distance,  $D_t$  from sensor reading in the sliding time window; estimates the two distance values,  $D_t^{ref}$  and  $D'_t$ , as well as the number of steps,  $N_t^{step}$  by analyzing the partition of  $D_t$ ; and finally computes  $FOGDOG_t$

where  $N^{max}$  is the maximum value of the number of steps and is set to  $5steps/sec$ . The first term,  $N_t^{step}/N^{max}$  detects abnormal cadence. While the normal cadence is  $1\sim 2step/sec$  during normal walking, the cadence of a user with FOG episodes is higher than the normal cadence. This causes  $FOGDOG_t$  to be amplified. The second term,  $(D_t^{ref} - D'_t)/D_t^{ref}$  evaluates how close the estimated HMD is to the reference distance within the sliding time window. After calculating  $FOGDOG_t$ , the system compares the  $FOGDOG_t$  value with the threshold to determine whether to activate the visual patterns.

Figure 23 summarizes the process of calculating  $FOGDOG_t$  from sensor readings during the sliding time window  $t$ .



**Figure 24.** Visual cues when the downward gaze angle is equal to (a)  $45^\circ$  and (b)  $90^\circ$ . The proposed system projects virtual cues consistently with the physical cues in the real world

### 4.3.3 Generation of Visual Patterns

The visual cue projected on the glasses consists of lines with the same color, e.g., blue lines. The interval between the lines is set to a half of the wearer's height times 0.855 in consideration of the glasses' vertical distance from the floor relative to the wearer's height. The width of the lines is  $0.5 \times 0.1 \text{ m}^2$  [70]. The maximum number of the lines is set to 5.

Figure 24 shows screenshots of the smart gait-aid system projecting visual cues. The system is initialized to give an effect as if real lines were regularly placed on the floor, and keeps refreshing the positions of lines based on the downward gaze angle and walking distance values. That is, the lines approach the PD user while walking and the intervals between the lines are adjusted when the downward gaze angle changes. Also, the system performs image processing when the wearer steps over the closest line such that the line passes by a foot and a new line appears as the last (fifth) line. To provide a perspective, the length of projected lines on the screen is set inversely proportional to the distance between the device and each line.



#### 4.4 Experiments

To evaluate our gait-aid system consisting of FOG detection and visual guidance functions, we obtained approval from an institutional review board (IRB) at Kyungpook National University Hospital, Daegu, Korea, and all patients signed their informed consent before the experiment. We recruited ten PD patients suffering from FOG, but are able to walk alone without any assistance, when they do not experience FOG. The details of the patients are tabulated in Table 4. They have, on average, a disease duration of 6.80 years, H-Y (Hoehn and Yahr) scale of 2.55, and UPDRS (Unified Parkinson's Disease Rating Scale scored by clinician) III score of 30.00. The experiments were performed at the Cerebroathia Center of Kyungpook National University Hospital, in the afternoon when more than 12 hours have passed after the last PD medication.

To evaluate the FOG detection capability via clinical trials with PD patients, we first collected data under the supervision of a clinician by conducting 5 Timed-Up-and-Go (TUG) tests [109] for each of 10 PD patients equipped with gait-aid glasses and ankle-

**Table 4.** PD patients for preliminary experiments having a disease duration of 6.80 years, H-Y (Hoehn and Yahr) scale of 2.55, and UPDRS (Unified Parkinson's Disease Rating Scale scored by clinician) III score of 30.00 on average

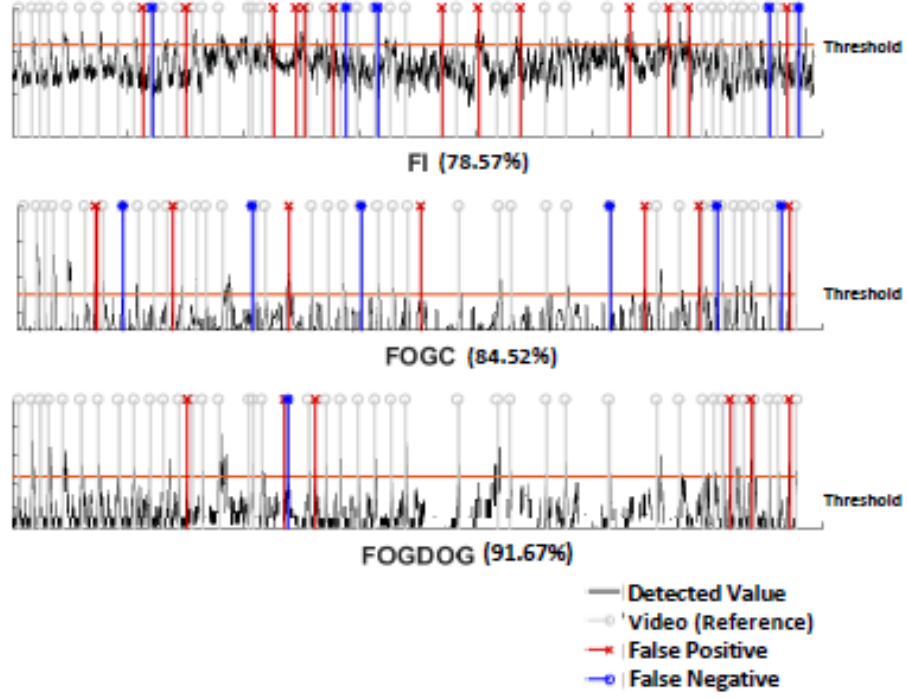
Subjects No.	Gender	Age	Disease Duration [year]	H-Y Scale	UPDRS III
P1	M	78	5	2.5	32
P2	M	76	8	3	38
P3	M	62	7	2	25
P4	F	59	4	3	32
P5	M	65	4	3	24
P6	F	79	8	3	22
P7	M	67	4	2	21
P8	F	73	14	2.5	32
P9	M	66	5	3	40
P10	M	83	9	2	34

worn sensors. The portions of collected data were then labeled as either FOG episodes or other activities (e.g., normal walking) after analyzing video recordings simultaneously captured during the experiments. As a result, the total amount of collected data corresponds to the duration of 1045s. The data contain 42 FOG episodes with total and average duration of 152 and  $3.62 \pm 2.91s$ , respectively. The ratio of the total FOG duration to the length of collected data was found to be 14.55%, and 80% of the FOG episodes were less than 5s. In addition to the 42 data sets of FOG episodes, we divided the entire data into 42 non-FOG data sets such that each data set has no more than 2 false positive cases.

Using the data from both PD patients, we evaluated FOGDOG, FI, and FOGC offline. We set the thresholds for FOGDOG and FOGC to 0.61 and 0.44, respectively. Each of these threshold values corresponds to an average minus two times the standard deviation where both average and standard deviation values are obtained from 10 independent trials of FOG episodes.

To evaluate the efficacy of our visual guidance system, the experiment first starts with a TUG test specified in a Parkinson's toolkit, where a patient (i) stands up from a chair when a clinical assistant says "Go"; (ii) walks along a straight lane of 3 meters; (iii) turns around; and (iv) comes back to the chair. Subsequently, the patient takes a 10-meter-walk test, in which a patient walks along a straight lane of 10 meters. The tests are performed with and without smart glasses by each of three PD patients.

When performing the TUG and 10-meter-walk tests with smart glasses, we provide each patient with two scenarios. The first one is based on a simplified scenario to provide visual cues moving horizontal stripe patterns at a steady speed, like *PD Glasses*. The visual cues are independent of wearer's movements and each stripe has regular intervals. The



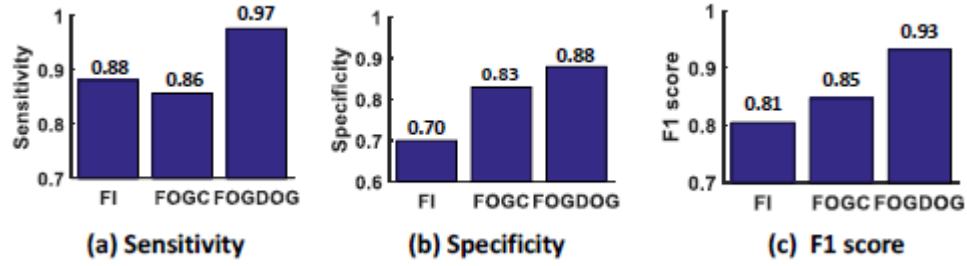
**Figure 25.** FOG detection of three methods over time: FI, FOGC and FOGDOG achieve 78.57%, 84.52% and 91.67% accuracy, respectively

second one employs our proposed method that displays a realistic visual cue. All tests were repeated twice. During the experiment, we record accelerometer data on a foot for precise measurements of the patient's gait speed and stride length. We then compute the elapsed time and the number of steps for each trial.

## 4.5 Results

### 4.5.1 FOG Detection Performance

We first compared the performance of FOGDOG with FI and FOGC by utilizing the data sets from real PD patients. Figure 25 depicts the FOG detection results of three methods (FI, FOGC, and FOGDOG) over time, plotting detected values and false positive/negative points. The analysis of detected values reveals that FOGDOG has a



**Figure 26.** FOG detection of three methods using: (a) sensitivity, (b) specificity, and (c) F1 scores. FOGDOG outperforms FI and FOGC by 9~18% and 5~11%, respectively

higher resolution than FI and FOGC in detecting FOG episodes, which in turn yields fewer false positive and false negative events. The quantitative analysis shows that the accuracy of FI, FOGC and FOGDOG are 78.57%, 84.52% and 91.67%, respectively, which demonstrates superior performance of FOGDOG.

For in-depth comparison, we used three performance metrics: sensitivity, specificity and F1 scores. The sensitivity (specificity) quantifies the proportion of positives (negatives) that are correctly identified as such, and hence, is computed as the ratio of the number of FOG (non-FOG) episodes correctly detected to the total number of FOG (non-FOG) data sets. The F1 score is the harmonic mean of precision and sensitivity where the precision is the number of true positives divided by the number of all positive results. As shown in Figure 26, the evaluation results demonstrate that the sensitivity, specificity, and F1 score values of FOGDOG are 0.97, 0.88, and 0.93, respectively, which are 9~11%, 5~18%, and 8~12% higher than others, respectively. This clearly indicates FOGDOG outperforms FI and FOGC.

#### 4.5.2 Gait-Aid Performance

As shown in Table 5, the patient's mobility is improved in both scenarios. The number of steps in the simplified scenario, which is associated with FOG, is decreased to 10.8% and 9.5% on average in each of TUG and 10-meter-walk tests. In the proposed scenario, the number of steps is decreased to 24.4% and 20.8%, respectively. The decreased number of steps means fewer FOG episodes occur. The average velocity of patients is improved by 15.3% and by 37.2% in the simplified and proposed scenarios, respectively. The average stride length is increased to 18.7% and 31.7% in the simplified and proposed scenarios, respectively.

Compared with the simplified scenario, in which PD patients simply recognize the horizontal line and walk, the proposed scenario helps the patient's efforts to step over the horizontal line, significantly improving their mobility. That is, the visual pattern that provides a perspective effectively improves the gait of people with PD. However, to obtain an effective perspective, the patient wearing the smart glasses needs to look downwards at

**Table 5.** The cueing effects of simplified and proposed scenarios on PD patients; compared with the baseline, the proposed scenario improves the average number of steps, velocity and stride length by 22.6%, 37.2% and 31.7%, respectively

	Number of steps	Velocity [cm/sec]	Stride length [cm]
<b>TUG test</b>			
Baseline (no glasses)	22.1±4.9	39.2±5.5	44.2±8.6
Simplified scenario	19.7±2.8	45.2±7.7	50.8±6.2
Proposed scenario	16.7±2.1	53.8±11.6	54.7±7.7
<b>10-meter-walk test</b>			
Baseline (no glasses)	22.1±2.6	80.2±2.3	62.5±5.3
Simplified scenario	20.0±1.3	95.2±8.7	74.1±7.0
Proposed scenario	17.5±1.7	105.7±8.6	84.7±9.0

45 to 90 degrees. Since it may be difficult for a patient who is not familiar with the use of the proposed system, pre-training would be needed to properly use the system.

The proposed gait-aid system displays the visual cue 1.1s after the occurrence of FOG since FOGDOG has to observe multiple steps to detect an FOG episode. However, this latency is acceptable because it is unnecessary (or undesirable) to detect and respond to a very short FOG event that lasts less than 1.1s.

#### **4.5.3 Discussion**

Although we can further improve this system in various aspects, e.g., real-time floor and obstacle detection, we observe that the computing capability of the smart glasses is not enough to implement such functions. Moreover, smart glasses are not enough to use the system all day long without recharging the battery. Thus, to minimize energy consumption, we design our visual guidance system such that it is automatically activated upon detection of FOG episodes or manually activated by the wearer depending on the need.

One patient who participated in the preliminary experiments said that he would feel more comfortable if his legs and feet are placed on an on-screen line as if the line is embedded on the floor and both patients responded positively to our smart gait-aid system as an assistance tool for PD patients. By contrast, several PD patients who refused to take part in our experiments due in part to technophobia were doubtful about the effectiveness of visual guidance. Most patients were afraid of fleeting attention when they are wearing glasses as also mentioned in other studies [71] [110].

It is important to get statistics for the types of the patient group such as gender, age, duration, H-Y scale and UPDRS III score since that gives physician (or other related people) the vital information for the prescription or in-depth research. In our evaluation, younger

woman (P4 in Table 4) exhibited better gait-performance than others, but that cannot prove the statistical meaning since there are not enough numbers of patients with PD to make statistics. So, we plan to recruit more patients with PD, and will validate our proposed system via comprehensive clinical trials and per-user analyses.

#### **4.6 Summary**

In this chapter, we develop a smart gait-aid system that can assist PD patients' gait when they experience FOG episodes. Our smart gait-aid system is comprised of an FOG episode detection system based on a sensor fusion technique and a visual guidance system based on markerless AR. The FOG episode detection system uses inertial sensors embedded in smart glasses and is optimized for limited processing capability of smart glasses. It achieves the accuracy of 83.7% in detecting FOG episodes according to our experiments. The visual guidance system also exploits the inertial sensors and processing capability of smart glasses to adaptively project visual cue patterns depending on the patient's gait speed and head direction. Since the visual guidance system is activated only when the patient experiences FOG episodes or needs a visual guidance, it is very energy-efficient. Our results of preliminary experiments demonstrate that when a patient wears the smart glasses to conduct TUG trials the average velocity and stride length are increased by 32.1% and 24.0%, respectively. In 10-meter-walk trials, the average velocity and stride length are increased by 24.1% and 45.3%, respectively. In the future, we will try to apply the machine-learning algorithm such as deep learning to detect and predict FOG episodes. Finally, we expect that our gait-aid system based on smart glasses can be adapted for and applied to the following diseases which accompany freezing: normal pressure

hydrocephalus (NPH), progressive supranuclear palsy (PSP), cortico basal degeneration (CBD), and strategic vascular lesion apart from PD [111].



## V. Conclusion

Optimization is the redesign of the existing complex system or technology to address the problems or constraint while maintaining the performance of existing knowledge or systems. Through the dissertation, we presented the three optimization methods (heuristic, learning-based and mathematical optimization) to meet the needs that arise when integrating facility-level healthcare systems into personal-level smart healthcare device (i.e., mobile POCT cell counting device, smart glasses). In chapter 2, we presented heuristic optimization that solves the problem of applying bench-top cell counting device based on software to battery-powered mobile POCT testing platforms. We have realized that there are many correlated cell template images to detect cell on source blood image, and that cells are ineffective to count cells and increase computational complexity. Through the heuristic optimization, we removed the ineffective cells and applied approximation search method. As a result, the optimized cell counting algorithm shown a performance error of 1% and a runtime of 11.5x faster. Based on that, we believe that the optimized cell counting algorithm will be available to diagnose some disease, such as HIV/AIDS, without restriction of time and place.

In the next chapter, based on learning-based optimization, we proposed NCC-CNN algorithm that solves the cell counting problem that is varying background brightness and out-focusing of lenses free in-line holographic device. The proposed algorithm uses NCC process to mark the cell as a candidate point and apply the CNN model distinguish the cell only at the points. Through the demonstration, we verified the proposed algorithm is capable of human-level cell counting ( $>0.95$ ). We hope that the proposed algorithm applies not only to cell counting, but also to the field of germ counting and further to the search

for the specific diseases (i.e. tumor cell, other moving cells). We plan to further extend this work to address another cell counting problem such as crowded cells in 3D dimension.

Last chapter introduced Gait-aid glasses for Parkinson's disease based on the mathematical optimization. In the details, we proposed a system integrated in two approaches which is FOGDOG and effective visual cue. For the FOGDOG to detect FOG, we optimized the existing mathematical model to achieve the constraint on the sudden long steps of wearer while FOG. And, we introduced the effective visual cueing pattern like actually on the floor. In the future, we will improve the system by combining learning-based optimization using deep learning with the handcraft models.

Through the whole chapters, we have shown that algorithm or system optimization is one of the key technologies for integrating the latest technologies into our lives for smart healthcare. However, these optimization is no limited to the healthcare field. For instance, many mid- and small-sized companies and even major companies are trying to solve the optimization problems to transform the advanced technologies to more practical things or products in our lives. In the future, we plan to work on the optimization not only in medical fields but also in various fields.

## Reference

- [1] Buntz, “Internet of Things institute.”, 2017 [Online]. Available: <http://www.ioti.com/iot-trends-and-analysis/2017-iot-still-next-big-thing-healthcare>.
- [2] Tractica, “Healthcare Wearable Device Shipments.”, 2016, [Online]. Available: <https://www.tractica.com/newsroom/press-releases/healthcare-wearable-device-shipments-to-reach-98-million-units-annually-by-2021/>.
- [3] Deloitte, “2017 global healthcare sector outlook.”, 2017, [Online]. Available: <https://www2.deloitte.com/global/en/pages/life-sciences-and-healthcare/articles/global-health-care-sector-outlook.html>.
- [4] Statista, “Projected CAGR for the global digital health market in the period 2015-2020, by major segment.”, 2015, [Online]. Available: <https://www.statista.com/statistics/387875/forecast-cagr-of-worldwide-digital-health-market-by-segment/>.
- [5] Kalarthi, Z.M., “A REVIEW PAPER ON SMART HEALTH CARE SYSTEM USING INTERNET OF THINGS.” *International Journal of Research in Engineering and Technology*, 2016, 05(03), pp. 80-84.
- [6] SAMSUNG Electronics, [Online]. Available: <https://www.samsung.com/us/mobile/wearables/>.
- [7] APPLE Inc., [Online]. Available: <https://www.apple.com/watch/>.
- [8] NIKE Inc., [Online]. Available: [https://www.nike.com/cdp/fuelband/us/en\\_us/](https://www.nike.com/cdp/fuelband/us/en_us/).
- [9] ADIDAS Inc., [Online]. Available: [https://www.nike.com/cdp/fuelband/us/en\\_us/](https://www.nike.com/cdp/fuelband/us/en_us/).
- [10] DIGITSOLE, [Online]. Available: <https://www.digitsole.com/>.
- [11] MOTIV, [Online]. Available: <https://mymotiv.com/>.
- [12] CCHIT, “Benefits of Healthcare Information Technology.” 2015, [Online]. Available: <https://www.cchit.org/benefits-of-healthcare-information-technology/>.
- [13] Mevvy, “mHealth Apps by Category 2015,” *IMS Institute for Healthcare informatics*, June 2015.

- [14] Pearl, R. "5 Things Preventing Technology Adoption In Health Care." *Forbes*, 11. SEP. 2015. [Online]. Available: <https://www.forbes.com/sites/robertpearl/2014/09/11/5-things-preventing-technology-adoption-in-health-care/#66873dda6889>.
- [15] Weise, T., "Global optimization algorithms-theory and application", *Self-published*, 2, 2009.
- [16] Rao, S.S., *Engineering Optimization: Theory and Practice*, Wiley, 2009.
- [17] UNAIDS, *UNAIDS Report on The Global AIDS Epidemic 2013*, 14 August 2014. [Online]. Available: <http://www.unaids.org/en/resources/documents/2013/name,85053,en.asp>.
- [18] Ra, H., Yoon, H., Son, S., and Park, T. "A robust cell counting approach based on a normalized 2D cross-correlation scheme for in-line holographic images." *Lab Chip*, 13, 2013, pp. 3398-3409.
- [19] Moon, S. Gurkan, U., Blander, J., Fawzi, W., Aboud, S., Mugusi, F., Kuritzkes, D., and Demirci, U. "Enumeration of CD4+ T-cells using a portable microchip count platform in Tanzanian HIV infected patients." *PLoS One*, 6, 2011, e21409.
- [20] Wang, Z., Chin, S., Chin, C., Sarik, J., Harper, M., Justman, J., and Sia, S. "Microfluidic CD4+ T-Cell Counting Device Using Chemiluminescence-Based Detection." *Anal. Chem.*, 82, 2009, pp. 36–40.
- [21] Ymeti, A., Li, X., Lunter, B., Breukers, C., Tibbe, A., Terstappen, L., and Greve, J. "A single platform image cytometer for resource-poor settings to monitor disease progression in HIV infection." *Cytom. Part A*, 2007, pp. 132-142.
- [22] Vanjari, L., Lakshmi, V., Teja, V., Subbalaxmi, M., Chandra, N., Ede, N., and Gadde, M. "Validation of a simple and cost-effective test for enumeration of CD4 cells." *JAIDS J. Acquir. Immune Defic. Syndr.*, 61, 2012, pp. 70-71.
- [23] Anderson, D.A., Crowe, S.M and Garcia, M., "Point-of-care testing." *Curr. HIV/AIDS Rep.*, 8, 2011, pp. 31-37.
- [24] Sjöström, P.J., Frydel, B.R., and Wahlberg, L.U. "Artificial neural network-aided image analysis system for cell counting," *Cytometry*, 36, 1999, pp. 18-26.

- [25] Forero, M.G., Kato, K., and Hidalgo, A. "Automatic cell counting in vivo in the larval nervous system of *Drosophila*." *Journal of Microscopy.*, 246, 2012, pp. 202-212.
- [26] Boyle, D.S., Hawkins, K.R., Steele, M.S., Singhal, M., and Cheng, X. "Emerging technologies for point-of-care CD4 T-lymphocyte counting." *Trends Biotechnol.*, 30, 2012, pp. 45-54.
- [27] Watkens, N.N., Sridhar, S., Cheng, X., Chen, G.D., Toner, M., Rodriguez, M., and Bashir, R. "A microfabricated electrical differential counter for the selective enumeration of CD4+ T lymphocytes" *Lab Chip.*, 11, 2011, pp. 1437-1447.
- [28] Hardeman, M.R., Dobbe, J.G.G., and Ince, C. "The laser assisted optical rotational cell analyzer (LORCA) as red blood cell aggregometer." in *Clin. Hemorheol. Microirc.*, 25, 2001, pp. 1-11.
- [29] Guck, J., Ananthakrishnan, R., Mahmood, H., Moon, T., and Cunningham, T. "The optical stretcher: A novel laser tool to micro manipulate cells." *Biophys. J.*, 81, 2001, pp. 767-784.
- [30] Cheng, X., Irimia, D., Irimia, M., Dixon, M., Sekine, K., Demirci, U., Zamir, L., Tompkins, R., Rodriguez, W., and Toner, M. "A microfluidic device for practical label-free CD4+ T cell counting of HIV-infected subjects." *Lab Chip.*, 7, 2007, pp. 170-178.
- [31] Qi, X., Xing, F., Foran, D., and Yang, L. "Robust segmentation of overlapping cells in histopathology specimens using parallel seed detection and repulsive level set." *IEEE Trans. Biomed. Eng.*, 59, 2012, pp. 754-765.
- [32] Mabey, D.C., Sollis, K.A., Kelly, H.A., Benzaken, A.S., Bitarakwate, E., Chantalucha, J., Chen, X.H., Yin, Y.P., Garcia, P., Strasser, S., Chintu, N., Pang, T., Terris-Prestholt, F., Sweeney, S., and Peeling, W. "Point-of-care tests to strengthen health systems and save newborn lives: The case of syphilis." *PLoS Med.*, 9, 2012, e1001233.
- [33] Breslauer, D., Maamari, R., Switz, N., Lam, W., and Fletcher, D. "Mobile phone based clinical microscopy for global health applications." *PLoS One*, 4, 2009, e6320.
- [34] Zhu, H., Sencan, I., Wong, J., Dimitrov, S., Tseng, D., Nagashima, K., and Ozcan, A. "Cost-effective and rapid blood analysis on a cell-phone." *Lab Chip.*, 13, 2013, pp. 1382-1288.

- [35] Rodriguez, W.R., Christodoulides, N., Floriano, P.N. Graham, S., Mohanty, S., Dixon, M., Hsiang, M., Peter, T., Zavahir, S., Thior, I., Romanovicz, D., Bernard, B., Goodey, A.P., Walker, B.D., and McDevitt, J.T. "A microchip CD4 counting method for HIV monitoring in resource-poor settings." *PLoS Med.*, 2, 2005, e182.
- [36] Nikolć, D., Muresan, R.C., Feng, W., and Singer, W. "Scaled correlation analysis: A better way to compute a cross-correlation." *Eur. J. Neurosci.*, 35, 2012, pp. 742-762.
- [37] Chan, Y. "Correlational analysis.," *Singapore Med. J.*, 44, 2003, pp. 614-919.
- [38] Schindelin, J., Rueden, C.T. Hiner, M.C., and Eliceiri, K.W. "The Image J ecosystem: An open platform for biomedical image analysis." *Molecular reproduction and development*, 82, 2015, pp. 518-529.
- [39] Xu, W., Jericho, M.H., Meinertzhagen, I.A., and Kreuzer, H.J. "Digital in-line holography for biological applications." *Proceedings of the National Academy of Sciences*, 98, 2001, pp. 11301-11305.
- [40] Garica-Sucerquia, J., Xu, W., Jericho, S.K., Klages, P., Jericho, M.H., and Kreuzer, H.J. "Digital in-line holographic microscopy." *Optical Society of America*, 98, 2006, pp. 836-850.
- [41] Greenbaum, A., Luo, W., Su, T., Göröcs, Z, Xue, L, Lsikman, S.O., Coskun A.F., Mudanyali, O., and Ozcan, A., "Imaging without lenses: achievements and remaining challenges of wide-field on-chip microscopy." *Nature methods*, 9, 2012, pp. 889-895.
- [42] Shiraki, A., Taniguchi, Y., Shimobaba, T., Masuda, N., and Ito, T., "Handheld and low-cost digital holographic microspopy." *physics.optics, arXiv*, 2012.
- [43] Bradury, L., "Segmentation of bright-field cell images." *Ph.D thesis*, University of Waterloo, Ontario, Canada, 2009, 54 pages.
- [44] Ali, R., Gooding, M., Szilágyi, T., Vojnovic, B., Christlieb, M., and Brady, M., "Automatic segmentation of adherent biological cell boundaries and nuclei from brightfield microscopy images." *Machine Vision and Application*, 23, 2012, pp. 607-621.
- [45] Drey, L.L., Graber, M.C., and Bieschke, J., "Counting unstained, confluent cells by modified bright-field microscopy." *Biotechniques*, 55, 2013.

- [46] Tikkanen, T., Ruusuvuori, P., Latnen, L., and Huttunen, H. "Training Based Cell Detection from Bright-Field Microscope Images." *9th International Symposium on Image and Signal Processing and Analysis (ISPA 2015)*, Zagreb, Croatia, 2015, pp. 160-164.
- [47] Dalal, N., and Triggs, B. "Histograms of Oriented Gradients for Human Detection." *IEEE Computer Vision and Pattern Recognition (CVPR) 2005*, San Diego, CA, USA, 2005, pp. 886-893.
- [48] Shu, C., Ding, X., and Fang, C. "Histograms of Oriented Gradients for Face Recognition." *Tsinghua Science & Technology*, 16, 2011, pp. 216-224.
- [49] Liimanainen, K., Ruusuvuori, P., Latonen, L., and Huttunen, H. "SUPERVISED METHOD FOR CELL COUNING FROM BRIGHT FIELD FOCUS STACKS." *Biomedical Imaging (ISBI), 2016 IEEE 13th International Symposium on. IEEE*, Prague, Czech Republic, 2016, pp. 391-394.
- [50] Salazar, D.A., Vélez, J.I., and Salazar, J.C. "Comaprision between SVM and Logistic Regression: Which One is Better to Discriminate?." *Revista Colombiana de Estadística*, 2012, pp. 223-237.
- [51] Ahn, D.H., Kim, N.S., Moon, S.J., Park, T., and Son, S.H. "Optimization of a Cell Counting Algorithm for Mobile Point-of-Care Testing Platforms." *Sensors*, 14(8), 2014, pp. 15244-15261.
- [52] Lewis, J. "Fast normalized corss-correlation." *Vision interface*, 1995.
- [53] Nikolić, D., Muresan, R.C., Feng, W., and Singer, W. "Scaled correlation analysis: a better way to compute a cross-correlogram." *European Journal of Neuroscience*, 35, 2012, pp. 742-762.
- [54] Chan, Y.H. "Correlational analysis." *Singapore Med*, 44, 2003, pp. 614-9.
- [55] Krizhevsky, A., Sutskever, I., and Hinton, G.E. "ImageNet Classification with Deep Convolutional Neural Networks." *Advances in neural information processing systems*, 2012, pp. 1097-1105.

- [56] Simonyan, K., and Zisserman, A. "VERY DEEP CONVOLUTIONAL NETWORKS FOR LARGE-SCALE IMAGE RECOGNITION." *arXiv*, 2014, arXiv.1409.1556.
- [57] Visin, F., Kastner, K., Cho, K., Matteucci, M., Courville, A., and Bengio, Y. "ReNet: A Recurrent Neural Network Based Alternative to Convolutional Networks." *arXiv*, 2015, arXiv:1505.00393.
- [58] Nair, V., and Hinton, G.E. "Rectified Linear Units Improve Restricted Boltzmann Machines." *Proceedings of 27th International Conference on Machine Learning*, 2010, pp. 807-814.
- [59] Memisevic, R., Zach, C., Pollefeys, M., and Hinton, G.E. "Gated Softmax Classification," *Advances in neural information processing systems*, 2010, pp. 1603-1611.
- [60] Blare, B., and Sarkar, S. "Background Subtraction in Varying Illuminations Using an Ensemble Based on an enlarged feature set." *Computer Vision and Pattern Recognition Workshops 2009 (CVPR 2009). IEEE Computer Society Conference on.*, Miami, FL, USA, 2009, pp. 66-73.
- [61] Apple Inc., [Online]. Available: <https://www.apple.com/kr/mac/>. [Access: 01 11 2017].
- [62] Braak, H., Ghebremedhin, E., Rüb, U., Bratzke, H., and Tredici, K.D. "Stages in the development of Parkinson's disease-related pathology." *emphCell*, 318, 2004, pp. 121-134.
- [63] European Parkinson's Disease Association 2011. [Online]. Available: <http://www.epda.eu.com/en/resources/life-with-parkinsons/part-1/prevalence-of-parkinsons-disease/>.
- [64] Parkinson's Disease Foundation. "Statistics on Parkinson's." 2015. [Online]. Available: <http://www.epda.eu.com/en/resources/life-with-parkinsons/part-1/prevalence-of-parkinsons-disease/>.
- [65] Berardelli, A., Rothwell, J.C., Thompson, P.D., and Hallett, M. "Pathophysiology of bradykinesia in Parkinson's disease." *Brain*, 124, 2001, pp. 2131-2146.



- [66] Morris, M. E., Huxham, F., McGinley, J., Dodd, K., and Iansek, R. "The biomechanics and motor control of gait in Parkinson disease." *Clin. Biomech.*, 16, 2001, pp. 459-470.
- [67] Jankovic, J. "Parkinson's disease: clinical features and diagnosis." *Journal of Neurology, Neurosurgery & Psychiatry*, 79(4), 2008, pp. 368-376.
- [68] Nutt, J. G., Bloem, B., Giladi, N., Hallett, M., Horak, F., and Nieuwboer, A. "Freezing of gait: Moving forward on a mysterious clinical phenomenon," *Lancet Neurol*, 10(8), 2011, pp. 734-744.
- [69] Moore, S. T., MacDougall, H. G., and Ondo, W. G. "Ambulatory monitoring of freezing of gait in Parkinson's disease," *J. Neurosci. Methods*, 167(2), 2008, pp. 340-348.
- [70] Park, H. K., Yoo, J. Y., Kwon, M., Lee, J. H., Lee, S. J., Kim, S. R., Kim, M. J., Lee, M. C., Lee, S. M., and Chung, S. J. "Gait freezing and speech disturbance in Parkinson's disease." *Neurol. Sci.*, 35(3), 2014, pp. 357-363.
- [71] McNaney, R., Vines, J., Roggen, D., Balaam M., Zhang, P., Poliakov, I., and Olivier, P. "Exploring the acceptability of google glass as an everyday assistive device for people with parkinson's." *In Proceedings of the SIGCHI Conference on Human Factors in Computing Systems*, Toronto, Ontario, Canada, May, 01, 2014, pp. 2551-2554.
- [72] Okuma, Y. "Practical approach to freezing of gait in Parkinson's disease." *Practical Neurology.*, 14(4), 2014, pp. 222-230.
- [73] Bloem, B. R., Hausdorff, J. M., Visser, J. E., and Giladi, Nir. "Falls and freezing of gait in Parkinson's disease: A review of two interconnected, episodic phenomena." *Movement Disorders*, 19, 2004, pp. 871-884.
- [74] Suteerawattananon, M., Morris, G. S. Etnyre, B. R., and Jankovic, J. "Effects of visual and auditory cues on gait in individuals with Parkinson's disease," *Journal of the Neurological Science*, 219(1), 2004, pp. 63-69.
- [75] Thaut, M. H., McIntosh, G. C., Rice, R. R., Miller, R. A., Rathbun, J., and Brault, J. M. "Rhythmic auditory stimulation in gait training for Parkinson's disease patients," *Movement Disorders*, 11(2), 1996, pp. 193-200.

- [76] Nieuwboer, A., Kwakkel, G., Rochester, L., Jones, D., Wegen, E., Willems, A. M., Chavret, F., Hetherington, V., Baker, K., and Lim I. "Cueing training in the home improves gait-related mobility in Parkinson's disease: the RESCUE trial," *Journal of Neurology, Neurosurgery & Psychiatry*, 78(2), 2007, pp. 134-140.
- [77] Hausdorff, J. M., Lowenthal, J., Herman, T., Gruendlinger, L., Peretz, C., and Giladi, N. "Rhythmic auditory stimulation modulates gait variability in Parkinson's disease," *European Journal of Neuroscience*, 26(8), 2007, pp. 2369-2375.
- [78] Allen, N. E., Sherrington, C., Suriyarachchi, G. D., Paul, S. S., Song, J., and Canning, C. G. "Exercise and motor training in people with Parkinson's disease: a systematic review of participant characteristics, intervention delivery, retention rates, adherence, and adverse events in clinical trials." *Parkinson's Disease*, vol. 2012, 2012, 15 pages.
- [79] Jovanov, E., Wang, E., Fredrickson, M., and Fratangelo, R. "deFOG-A Real Time System for Detection and Unfreezing of Gait of Parkinson's Patients." *In Proceedings of the Annual International Conference of the IEEE Engineering in Medicine and Biology Society (EMBC)*, Minneapolis, MN, USA, 2009, pp. 5151-5154.
- [80] Baram, Y. "Virtual sensory feedback for gait improvement in neurological patients." *Frontiers in Neurology*, 4, 138, 2013.
- [81] Bachlin, M., Poltnik, M., Roggen, D., Maidan, I., Hausdorff, J. M., Giladi, N., and Troster, G. "Wearable assistant for Parkinson's disease patients with the freezing of gait symptom." *IEEE Transactions on Information Technology in Biomedicine*, 14, 2010, pp. 436-446.
- [82] Lee, S. J., Yoo, J. Y., Ryu, J. S., Park, H. K., and Chung, S. J. "The effects of visual and auditory cues on freezing of gait in patients with Parkinson's disease." *American Journal of Physical Medicine & Rehabilitation*, 91, 2012, pp. 2-11.
- [83] Chong, R. K., Lee, K. H., Morgan, J. Mehta, S., Griffin, J., Marchant, J., Searle, N., Sims, J., and Sethi, K. "Closed-Loop VR-Based Interaction to Improving Walking in Parkinson's Disease." *Journal of Novel Physiotherapies*, 1, 2011, 101 pages.

- [84] Chong, R. K., Lee, K. H., Morgan, J., and Wakade, C. "Duration of step initiation predicts freezing in Parkinson's disease." *Acta Neurologica Scandinavica*, 132, 2015, pp. 105-110.
- [85] Tomlinson, C. L., Stowe, R., Patel, S., Rick, C., Gray, R., and Clarke, C. E. "Systematic review of levodopa dose equivalency reporting in Parkinson's disease." *Movement Disorders*, 25, 2010, pp. 2649-2653.
- [86] Fahn, S. "Parkinson disease, the effect of levodopa, and the ELLDOPA trial." in *Archives of Neurology*, 56, 1999, pp. 529-535.
- [87] Fahn, S., Oakes, D., Shoulson, I., Kieburtz, K., Rudolph, A., Marek, K., Seibyl, J., Lang, A., Olanow, C. W., Tanner, C., Chifitto, G., Zhao, H., Reyes, L., Shinaman, A., Comella, C., Goetz, C., Blasucci, L., Samanta, J., Stacy, M., and Williamson, K. "Levodopa and the progression of Parkinson's disease." in *N. Engl. J. Med.*, 351, 2004, pp. 2498-2508.
- [88] Rodriguez-Oroz, M. C., Obeso, J. A., Lang, A. E., Houeto, J.-L. Pollak, P., Rehncrona, S., Kulisevsky, J., Albanes, A., Volkmann, J., Quinn, M.I.H.P., Speelman, J. D., Guridi, J., Zamabide, I., Ginonell, A., Moet, J., Pascual-Sedano, B., Pidoux, B., Bonnet, A. M., Agid, Y., Xie, J., Benabid, A.-L., Lozano, A. M. Saint-Cyr, J., Romito, L., Cantarino, M. F., Serrati, M., Fraix, V., and Blercom, N. V. "Bilateral deep brain stimulation in Parkinson's disease: a multicentre study with 4 years follow-up." *Brain*, 128, 2005, pp. 2240-2249.
- [89] Deuschl, G., Schade-Brittinger, C., Krack, P., Volkmann, J. Schäfer, H., Bötzel, K., Daniels, C., Deutschländer, A., Dillmann, U, Eisner, W., Gruber, D., Hamel, W., Herzog, J., Hilker, R., Klebe, S., Kloß, M., Koy, J., Krause, M., Kupsch, A., Lorenz, D., Lorenzl, S., Mehdorn, M., Moringlane, J., Oertel, W., Pinsker, M. O., Reichmann, H., Reuß, A., Schneider, G.-H., Schnitzler, A., Steude, U., Sturm, V., Timmermann, L., Tronnier, V., Trottenberg, T., Wojtecki, L., Wolf, E., Poewe, W., and Voges, J. "A randomized trial of deep-brain stimulation for Parkinson's disease," *N. Engl. J. Med.*, 355, 2006, pp. 896-908.

- [90] Moore, S. T., Yungher, D. A., Morris T. R., Dilda V., MacDougall, H. G., Shine, J. M., Naismith S. L., and Lewis, S. J. G. "Autonomous identification of freezing of gait in Parkinson's disease from lower-body segmental accelerometry," *Journal of Neuroengineering and Rehabilitation*, 10, 2013, pp. 10-19.
- [91] Niazmand, K., Tonn K., Zhao Y., Fietzzek U. M., Schroeteler, F., Ceballos-Baumann, A. O., and Lueth, T. C. "Freezing of gait detection in parkinson's disease using accelerometer based smart clothes," *In Proceedings of the Biomedical Circuits and Systems Conference (BioCAS)*, San Diego, CA, USA, 10-12, November, 2011, pp. 201-204.
- [92] Coste, C. A., Sijobert, B., Pissared-Gibollet, R., Pasquier, M., Esiau, B., and Geny, C. "Detection of Freezing of Gait in Parkinson Disease: Preliminary Results." *Sensors*, 14, 2014, pp. 6819-6827.
- [93] Tripoliti, E. E., Tzallas, A. T., Tsipouras, M. G., Rigas, G., Bougia, P., Leontiou, M., Konisiotis, S., Chondrogiorgi, M., Tsouli, S., and Fotiadis, D. I. "Automatic detection of freezing of gait events in patients with Parkinson's disease." *Computer Methods and Programs in Biomedicine*, 110(1), 2013, pp. 12-26.
- [94] Pepa, L., Verdini, F., Capecci, M., Gabriella, M., and Leo, T. "Can the current mobile technology help for medical assistance? The case of freezing of gait in Parkinson disease," *Ambient Assisted Living*, 2014, pp. 177-185.
- [95] Mazilu, S., Blanke, U., Dorfman, M., Gazit, E., Mirelman, A., Hausdoff, J. M., and Tröster, G. "A Wearable Assistant for Gait Training for Parkinson's Disease with Freezing of Gait in Out-of-the-Lab Environment." *ACM Transactions on Interactive Intelligent Systems (TiiS)*, 5(1), 5, 2015, pp. 5:1-31.
- [96] Miyake, Y. "Interpersonal Synchronization of Body Motion and the Walk-Mate Walking Support Robot." *IEEE Transactions on Robotics*, 25, 2009, pp. 638-644.
- [97] McIntosh, G. C., Brown, S. H., Rice, R. R., and Thaut, M. H. "Rhythmic auditory-motor facilitation of gait patterns in patients with Parkinson's disease," *Journal of Neurology, Neurosurgery & Psychiatry*, 62, 1997, pp. 22-26.

- [98] Snijders A. H., Warrenburg B. P., Giladi, N, and Bloem, B. R. "Neurological gait disorders in elderly people: clinical approach and classification," *Lancet Neurology*, 6, 2007, pp. 63-74.
- [99] Hove, M. J., Suzuki, K., Uchitomi, H., Orimo, S., and Miyake, Y. "Interactive Rhythmic Auditory Stimulation Reinstates Natural 1/f Timing in Gait of Parkinson's Patients," *PLoS ONE*, 7, 2012, e32600.
- [100] Stern, G. M., Lander, C. M., and Lees, A. J. "Akinetic freezing and trick movements in Parkinson's disease," *In Current Topics in Extrapyrmidal Disorders*, 1980, pp. 137-141.
- [101] Kompolti, K., Goetz, C. G., Leurgans, S., Morrissey, M., and Siegel, M. "On Freezing in Parkinson's Disease: Resistance to Visual Cue Walking Devices," *Movement Disorders*, 15, 2000, pp. 309-312.
- [102] Ferrarin, M., Brambilla, M., Garavello, L., Candia, A. D., Pedotti, A., and Rabuffetti, M. "Microprocessor-controlled optical stimulating device to improve the gait of patients with Parkinson's disease," *Medical Biological Engineering Computing*, 42, 2004, pp. 328-332.
- [103] YouTude, "PD Glasses - Visual cues for walking with Parkinson's Disease." 2014, [Online]. Available: [https://www.youtube.com/watch?v=izaGU\\_khU1Y](https://www.youtube.com/watch?v=izaGU_khU1Y).
- [104] Gallagher, R., Werner, W. G., Damodaran, H., and Deutsch, J. E. "Influence of cueing, feedback and directed attention on cycling in a virtual environment: Preliminary findings in healthy adults and persons with Parkinson's disease." *IEEE International Conference on Virtual Rehabilitation (ICVR)*, Valencia, Spain, 2015, pp. 11-17.
- [105] Skog, I., Nilsson, J.-O., and Händel, P. "Evaluation of Zero-Velocity Detectors for Fott-Mounted Inertial Navigation Systems." *International conference on indoor positioning and indoor navigation (IPIN)*, Zurich, Switzerland, 2010.
- [106] Almeida, Q. J., and Lebold, C. A. "Freezing of gait in Parkinson's disease: a perceptual cause for a motor impairment?." *J. Neurology, Neurosurgery & Psychiatry*, 81, 2010, pp. 513-518.

- [107] Madgwick, S. O. H., Harrison, A. J. L., and Vaidyanathan, R. "Estimation of IMU and MARG orientation using a gradient descent algorithm," *IEEE International Conference on Rehabilitation Robotics (ICORR)*, Zurich, Switzerland, 2011.
- [108] Bland, J. M., and Altman, D. G. "Measuring agreement in method comparison studies." *Statistical Methods in Medical Research*, 8, 1999, pp. 135-160.
- [109] Bohannon, R. W. "Reference Values for the Timed Up and Go Test: A Descriptive Meta-Analysis." *Journal of Geriatric Physical Therapy*, 29, 2006, pp. 64-68.
- [110] Zhao, Y., Heida, T., van Wehen, E. E. H., Bloem, B. R., and van Vezel, R. J. A. "E-health Support in People with Parkinson's Disease with Smart Glasses: A Survey of User Requirements and Expectations in the Netherlands." *Journal of Parkinson's Disease*, 5, 2015, pp. 369-378.
- [111] Fahn, S. "The freezing phenomenon in parkinsonism." *Negative motor phenomena*, 1995, pp. 53-63.

## 요 약 문

### Optimization Algorithms for Integrating Advanced Facility-Level Healthcare Technologies into Personal Healthcare Devices

본 논문은 의료 관련 연구시설 및 병원 그리고 실험실 레벨에서 사용되는 전문적인 헬스케어 시스템을 개인의 일상생활 속에서 사용할 수 있는 스마트 헬스케어 시스템에 적용시키기 위한 최적화 문제에 대해 다룬다. 현대 사회에서 의료비용 증가 세계적인 고령화에 따라 의료 패러다임은 질병이 발생한 뒤 시설 내에서 치료 받는 방식에서 질병이나 건강관리에 관심있는 환자 혹은 일반인이 휴대할 수 있는 개인용 디바이스를 이용하여 의료 서비스에 접근하고, 이를 이용하여 질병을 미리 예방하는 방식으로 바뀌었다. 이에 따라 언제, 어디서나 스마트 디바이스(스마트폰, 스마트워치, 스마트안경 등)를 이용하여 병원 수준의 예방 및 진단을 실현하는 스마트 헬스케어가 주목 받고 있다. 하지만, 스마트 헬스케어 서비스 실현을 위하여 기존의 전문 헬스케어 장치 및 과학적 이론을 스마트 디바이스에 접목하는 데에는 스마트 디바이스의 제한적인 컴퓨팅 파워와 배터리, 그리고 연구소나 실험실에서 발생하지 않았던 환경적인 제약조건으로 인해 적용 할 수 없는 문제가 있다. 따라서 사용 환경에 맞춰 동작 가능하도록 최적화가 필요하다. 본 논문에서는 Cell counting 분야와 파킨슨 환자의 보행 보조 분야에서 전문 헬스케어 시스템을 스마트 헬스케어에 접목시키는데 발생하는 세 가지 문제를 제시하고 문제 해결을 위한 세 가지 최적화 알고리즘(Heuristic optimization, Learning-based optimization, Mathematical optimization) 및 이를 기반으로 하는 시스템을 제안한다.

핵심어: Optimization, Smart Healthcare, Cell Counting, Parkinson's disease, System Integration.